How to cite: Chen Y, Nan Z, Cao Z, Ou M, Feng K. A stepwise framework for interpolating land surface temperature under cloudy conditions based on solar-cloud-satellite geometry. ISPRS Journal of Photogrammetry and Remote Sensing. 2023, 197: 292-308. doi:10.1016/j.isprsjprs.2023.02.004.

A stepwise framework for interpolating land surface temperature under cloudy conditions based on the solar-cloud-satellite geometry

Yuhong Chen[1], Zhuotong Nan[1,2*], Zetao Cao[1], Minyue Ou[1], Keting Feng[3,4]

1 Key Laboratory of Ministry of Education on Virtual Geographic Environment, Nanjing Normal University, Nanjing, 210023, China

2 Jiangsu Center for Collaborative Innovation in Geographical Information Resource Development and Application, Nanjing, 210023, China

3 Northwest Institute of Eco-Environment and Resources, Chinese Academy of Sciences, Lanzhou, 730000, China

4 National Cryosphere Desert Data Center, Lanzhou, 730000, China

Corresponding author: Zhuotong Nan, nanzt@njnu.edu.cn

Abstract: Thermal infrared land surface temperature (LST) data from satellites often contain extensive missing values due to high cloudiness degree, which severely hinders their use in applications. Despite the many methods developed, common methods, such as fusion with microwave or reanalysis data and the surface energy budget approach, still remain subject to important limitations and uncertainties, such as dependency on coarse resolution data and difficulty in interpolation for large-scale missing LST data. In this study, we proposed a stepwise framework for estimating missing cloudy-sky LST values of Moderate Resolution Imaging Spectroradiometer (MODIS) from informative samples owing to the solar-cloud-satellite geometry (SCSG) effect, by which satellite imagery records the cloudy-sky LST values of a portion of pixels. We first estimated the clear-sky LST equivalents for all cloud-affected pixels via a similarity-based approach and then

determined unknown LSTs for cloudy pixels by training a machine-learning model on cloudy-sky LST values observed owing to the SCSG effect. We demonstrated the utility of this approach by using MODIS/Aqua daytime LST data over Qinghai-Tibet Plateau (QTP) and validated the interpolation results against representative *in-situ* LST observations and two recently published all-weather LST datasets. When compared to the corresponding *in-situ* measurements, the interpolated cloudy-sky LST values showed satisfactory accuracy with a mean absolute error (MAE) value of 3.99 ºC and a coefficient of determination (R^2) value of 0.74, while the MODIS/Aqua clear-sky LST values led to an MAE value of 2.66 ºC and an R^2 value of 0.86. Compared to the two all-weather LST datasets, results of this study showed the highest accuracy over the data-gap-filled regions in terms of all quantitative performance metrics, more natural transition textures, and better representation of seasonal characteristics. The proposed framework has the advantage of relying on the MODIS family data and handling extensive missing data as well as triggers opportunities to leverage the SCSG effect to produce high-quality all-weather LST data.

Key words: land surface temperature (LST); solar-cloud-satellite geometry (SCSG); clear-sky LST equivalent; stepwise interpolation framework; cloud-contaminated pixels.

1. Introduction

Land surface temperature (LST) is an important variable related to surface energy and water balance at the local-to-global scales and is controlled by a complex interplay of topography, incident radiation, atmospheric processes, hydrology, and land use and land cover (Anderson et al., 2008; Brunsell and Gillies 2003; Kustas and Anderson 2009; Li et al., 2013). Globally, satellite remote-sensing data continuously provide spatiotemporal coverage at the fine-to-coarse resolutions for LST (Tomlinson et al., 2011). Since satellite LST data can only be effectively retrieved from thermal

infrared (TIR) measurements under clear sky conditions, large areas of data gaps may occur due to missing values when the surface is obscured by clouds. Cloudy skies account for more than half of day-to-day weather conditions across the world (Hagihara et al., 2011). There is a growing demand for the development of effective cloud-removal algorithms for satellite LST products as the scarcity of high-quality all-weather LST data has severely limited hydrometeorological studies and the application of process-based models on the regional-to-global scale.

Many algorithms have been developed to recover missing LST values caused by cloud cover, such as microwave-based methods (Shwetha and Kumar 2015; Tang et al., 2022; Xu and Cheng 2021), surface energy balance (SEB)-based methods (Jin 2000; Martins et al., 2019; Yang et al., 2019; Yu et al., 2019), and data fusion approaches (Long et al., 2020; Zhang et al., 2021; Zhao and Duan 2020). Some studies have attempted to interpolate cloud-free LST values from the neighborhood pixels with similar environmental characteristics to missing cloudy-sky ones (Chen et al., 2021; Collins et al., 2020; Li et al., 2018; Yu et al., 2015). However, the interpolation of these cloud-free LST values can lead to clear-sky biases with respect to actual cloudy-sky conditions (Collins et al., 2020; Ermida et al., 2019). Advantageous compared to infrared signals, microwave signals penetrate clouds and are less affected by atmospheric absorption while acquiring LST under all-sky conditions (Duan et al., 2020; Palaniyandi et al., 2021). However, microwave data suffer from a coarse spatial resolution and are very sensitive to surface conditions, such as soil moisture, surface roughness, and vegetation cover, thus resulting in large uncertainties in LST data (Duan et al., 2020; Prigent et al., 2016). SEB-based methods leverage the surface energy balance equation to calculate the difference in surface radiation flux between clear and cloudy sky conditions and then estimate missing LST values by accounting for the differences (Jia et al., 2021; Lu et al., 2011; Yu

et al., 2019). The SEB-based methods require ancillary data (e.g., wind speed, air temperature, and energy fluxes), the accuracy of which greatly affects the interpolation performance (Martins et al., 2019). Recently, some studies have successfully merged remotely sensed TIR LST data with reanalysis data to generate all-weather LST data (Dumitrescu et al., 2020; Long et al., 2020; Zhang et al., 2021). In general, LST data products fused with reanalysis data are subject to large uncertainties as reanalysis data have a coarser spatial resolution than do TIR LST data as well as low accuracy (Mo et al., 2021). This is in particular true for remote areas with complex terrains and sparsely distributed *in-situ* observation sites, which in turn adversely affect the final accuracy of the fused products.

In-situ observations provide the most reliable cloudy-sky LST values, thus playing a pivotal role in the validation of interpolated cloudy-sky LST data as well as the development of plausible methods to recover missing LST values. Tan et al. (2021) used *in-situ* LST data to calculate the cloudiness-induced biases in satellite LST before applying them to the recovery of cloudy-sky LST. There exist various difficulties in practice, such as an insufficient number of measurement sites and the issue of a spatial scale mismatch between *in-situ* observations and satellite observations (Coll et al., 2005; Li et al., 2013; Wan 2008). For example, for l-km LST data from the Moderate Resolution Imaging Spectroradiometer (MODIS), suitable *in-situ* observation sites should be both at least 5 km × 5 km in size and homogeneous (Wan 2008). Since few sites can meet these requirements, the use of *in-situ* observations to retrieve cloud-affected LST values remains limited.

Owing to the solar-cloud-satellite geometry (SCSG) effect, there is an alternative way to compensate for the apparent weaknesses of *in-situ* observations. Since the sun and satellites have specific illumination and observation angles with respect to the ground, cloudy regions identified

by satellites do not exactly match the areas where clouds actually obstruct solar radiation. This effect is referred to as the solar-cloud-satellite geometry effect (Wang et al., 2017). Therefore, some regions where solar radiation is shadowed by clouds can be directly observed by satellites (Baraldi and Tiede 2018; Wang et al., 2017), through which the LST values of cloudy pixels can be known. The cloudy LST values interpolated via the satellite retrieval algorithm may have biases compared to the actual values due to the use of clear-sky parameters. Cloudy pixels with known LST values owing to the SCSG effect could be useful as they can provide many samples with cloud effects at the same resolution.

In this study, we proposed a stepwise framework to estimate missing LST values based on cloudy pixels with known LST values owing to the SCSG effect. Based on observation geometry, an LST image can be partitioned into the following four regions: two clear-sky regions and two cloudy-sky regions, with each containing a region with missing LST values (Wang et al., 2019). First, clear-sky LST equivalents were estimated for all cloud-affected pixels via a similarity-based approach (Chen et al., 2021). Finally, the missing cloudy-sky LST values were estimated by training a machine-learning model on cloudy-sky pixels with known LST values and on clear-sky equivalents already prepared. This framework is flexible enough to accommodate any existing clear-sky interpolation approach in the first step (Chen et al., 2021; Metz et al., 2014; Neteler 2010; Yu et al., 2015) as well as suitable machine-learning algorithms in the final step.

2. Process of the framework

2.1. Overall framework of the SCSG-based approach

The satellite and sun have specific illumination and observation angles with respect to the

ground. When a surface is covered by clouds, a special observation geometry known as the SCSG forms (Wang et al., 2019). Based on the SCSG effect (Wang et al., 2019), each MODIS LST image was partitioned into four SCSG regions (A, B, C, and D) based on the cloud-top height and sun/satellite illumination/view angles provided by the MODIS data family (see Section 2.2). Regions A and B were under clear skies, whereas regions C and D were under cloudy skies. The LST values were known in regions A and D but unknown in B and C, which were to be predicted via interpolation. Cloudy region D with known LST values was of great significance for providing samples to recover unknown LST values under cloudy skies.

The proposed interpolation framework leveraged the SCSG effect to interpolate for missing LST values in the MODIS LST products. Fig. 1 illustrates the general workflow of this study, consisting of four steps. First, MODIS LST images were partitioned into the four SCSG regions (Wang et al., 2017; Wang et al., 2019) (Fig. 1a). Though known, the LST values in cloudy region D may be biased due to the use of clear-sky parameters in the LST inversion algorithm. This study relied on *in-situ* observations at representative sites in order to reduce LST biases in region D. Second, a clear-sky interpolation method with the advantage of effectively handling large data gaps (Chen et al., 2021) was employed to estimate the clear-sky LST equivalents for every pixel in regions B, C, and D (Fig. 1b). The clear-sky LST equivalents in region B well approximated the true clear-sky LST values in this region, whereas the equivalents in regions C and D were needed to recover the missing cloudy LST values in region C.

Third, the LST values in region C were estimated (Fig. 1c). This was carried out under the assumptions that there existed pixels in region D with high similarity to each missing cloudy-sky pixel in region C in order to determine cloud effects on the LST as well as that both shared the same

prediction model representing the cloudy-sky LST value as a function of environmental factors and clear-sky LST equivalent. In practical applications, this approach first spatially divides the pixels in region C into many clusters based on environmental predictors to boost computational efficiency. Second, a machine-learning model, multivariate adaptive regression splines (MARS) in the present study, is trained for each cluster with the region D pixels that were identified as similar to the cluster centroid, for which clear-sky LST equivalents, cloudy-sky corrected LST values, and environmental predictors are readily known. Finally, these prediction models are applied on a cluster-by-cluster basis to the region C pixels in order to determine the missing cloud-sky LST values, provided that the values of environmental predictors are available.

After these three steps are completed, an all-weather LST image is generated. In the last step (Fig. 1d), this study also tested the accuracy and precision of the generated all-weather LST images based on both visual inspection and quantitative performance metrics. To better describe the process involved, the following subsections explain the image partitioning based on the SCSG effect in Section 2.2; the bias correction of cloudy-sky LST values in region D in Section 2.3; the estimation of clear-sky equivalents in regions B, C, and D in Section 2.4; and the recovery of missing cloudy-sky LST values in region C in Section 2.5.

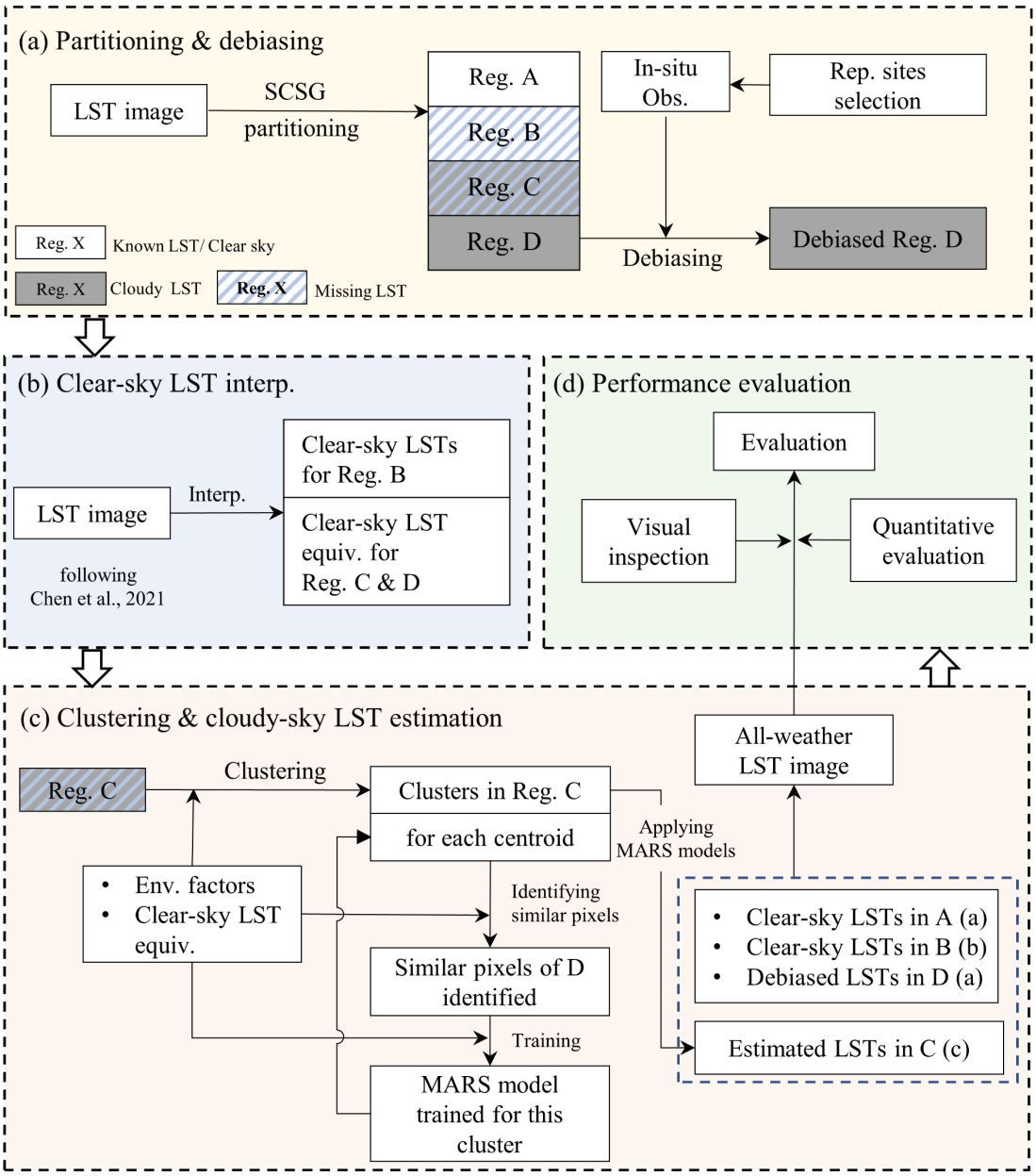

Fig. 1 The workflow of interpolating missing values of satellite land surface temperature (LST) based on the solar-cloud-satellite geometry (SCSG) effect. (a) Partitioning of the Moderate Resolution Imaging Spectroradiometer (MODIS) LST image based on the SCSG effect. Region A was under clear sky with known LST values. Regions B and C had missing LST pixels; region B was under clear sky, whereas region C was under cloudy sky. Region D was under cloudy sky with known LST values. Due to the use of the clear-sky parameter in the LST inversion algorithm, observed LST values in region D were most likely to be biased unless corrected by *in-situ* observations at representative sites. (b) Implementation of

a clear-sky LST interpolation method following Chen et al. (2021) for pixels in regions B, C, and D. (c) Recovery of missing LST values in region C via multivariate adaptive regression splines (MARS) trained on the region D pixels with bias-removed cloudy-sky LST values. An all-weather LST image was obtained by assembling all the processed SCSG regions. (d) Evaluation of the all-weather LST image via visual inspection and quantitative performance metrics.

2.2. Image partitioning based on the SCSG effect

Fig. 2 illustrates the concept of the SCSG effect. Based on this effect, MODIS LST images were partitioned into the following four regions: region A was clear-sky with valid satellite LST observations; region B was clear-sky with no known LST; region C was cloud-obscured with no known LST; and region D was cloud-obscured with known LST owing to the visible viewing angle from the satellite to the surface. When the satellite viewing zenith/azimuth angles, solar zenith/azimuth angles, and cloud-top height are known, the cloud shadow positions on the ground can be calculated from the observation geometry (Fig. 2) as follows (Wang et al., 2019):

$$\begin{cases} X_{pro} = X_{map} + H\,tan\,\theta_v\,sin\,\varphi_v \\ Y_{pro} = Y_{map} + H\,tan\,\theta_v\,cos\,\varphi_v \end{cases} \tag{1}$$

$$\begin{cases} X_{shw} = X_{pro} - H\,tan\,\theta_s\,sin\,\varphi_s \\ Y_{shw} = Y_{pro} - H\,tan\,\theta_s\,cos\,\varphi_s \end{cases} \tag{2}$$

where (X_{map}, Y_{map}) is the position of the cloud in a satellite LST image and is probably a pseudo position within regions B or C; (X_{pro}, Y_{pro}) is the orthographic projection of cloud onto the surface; and (X_{shw}, Y_{shw}) is the actual cloud shadow region where clouds obstructed solar radiation and formed regions C and D; H is the cloud-top height above the surface, determined by subtracting the surface altitude from the cloud-top height provided by the MODIS Level-2 cloud product (MOD/MYD06_L2); θ_v and φ_v are the satellites observing the zenith and azimuth angles,

respectively; and θ_s and φ_s are the solar zenith and azimuth angles, respectively.

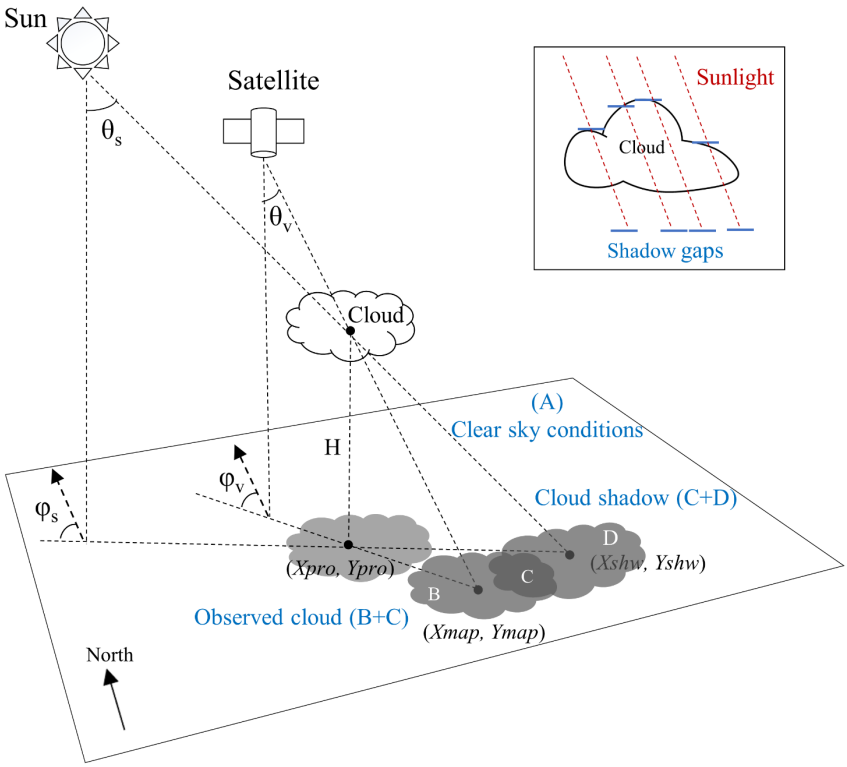

Fig. 2 Illustration of the SCSG effect shown on a satellite LST image, as modified from Wang et al. (2019). Region A was under clear sky. Regions B and C were obscured by clouds from the satellite view, shown in an LST image as missing pixels (X_{map}, Y_{map}). Regions C and D were the actual shadow regions (X_{shw}, Y_{shw}), but region D was visible from the satellite and had known LST values. Please refer to Eqs. (1) and (2) for the abbreviations and symbols used. The inset shows the shadow gaps on the LST image resulting from the large difference in cloud-top height between nearby cloud-covered pixels.

The steps to partition a MODIS LST image into the SCSG regions are presented below:

1) Smoothing pixelated data of cloud-top height

A giant cloud body is not homogeneous everywhere and varies in cloud-top height. The MODIS instrument records spatially continuous cloud-top heights with many numerically discrete pixel-by-pixel heights. In this case, if the height difference between two adjacent cloudy pixels is

large, shadow gaps can appear on the surface according to Eqs. (1) and (2) (see inset in Fig. 2), when sunlight illuminates the cloud top at certain zenith angles. Shadow gaps are unreasonable for intrinsically continuous cloud bodies (Wang et al., 2019). To address this issue, the MODIS cloud-top height data were smoothed by using a mean filter with a 15 × 15 window. Although Wang et al. (2019) suggested a 7 × 7 window for smoothing cloud-top height data over Qinghai-Tibet Plateau (QTP), after many trials, a window of 15 × 15 was preferred in this study, because it allowed for more effective reduction of data gaps without a significant degradation in accuracy due to the wider window.

2) Partitioning an LST image into SCSG regions

Based on the cloud positions detected by the satellite (X_{map}, Y_{map}) and the sun/satellite illumination/view angles (φ_v, φ_s, θ_v, θ_s), the orthographic cloud projection onto the surface (X_{pro}, Y_{pro}) can be estimated from Eq. (1). The cloud shadow positions (X_{shw}, Y_{shw}), where solar radiation is obstructed by clouds, can be calculated from Eq. (2). All shadow pixels whose LSTs were observed were classified into region D, otherwise into region C. Region A consisted of pixels with known LST, except for those already in region D. The remaining pixels whose LSTs were unknown, except for those already in region C, constituted region B; but some of whose cloud-top heights recorded by the satellite were lower than their altitudes were reassigned to region C.

3) Post-processing to eliminate anomalies

As shown in Fig. 3 there were some anomalies in the resulting SCSG images, such as MODIS/Aqua daytime LST image on day 18 of 2003 over a subregion of QTP. In this study, the three main types of anomalies (illustrated by R1, R2, and R3 in Fig. 3a) were removed by post-processing the resulting SCSG images, as described below.

The anomalies shown in subregion R1 (Fig. 3a) were related to the process of smoothing the cloud-top height data, in particular, over a large cloudy area, thus resulting in misclassification in the SCSG images. These anomalies appeared to be a few region B pixels surrounded by region C pixels. To resolve this issue, we applied a 5 × 5 moving window to each region B pixel and reclassified the pixel based on a majority rule within the window. The size of the moving window was determined via visual inspection to minimize the occurrence of such anomalies in the resulting image, as shown in subregion R1 in Fig. 3b.

The second type of anomaly was caused by a discontinuity in viewing/solar angle data, where two MODIS scans overlapped (e.g., subregion R2 in Fig. 3a). The overlaps can be identified by abrupt changes between adjacent pixels in the MODIS angular image. Therefore, we subtracted the angular image from a new image created by shifting the angular image by one column to the right and applied a threshold of 100° to the resulting difference image to detect the affected pixels. Then, pixels near the affected pixels were processed by using a moving window with a majority-voting scheme.

Subregion R3 in Fig. 3a shows anomalies due to small data gaps in the MODIS instrumental coverage from the equator to 50° latitude as well as coverage overlapping from 50° latitude poleward (Masuoka et al., 1998). Since these gaps did not contain adequate information to accurately classify the SCSG region, we roughly classified them as region C if they were acquired in spring and summer, when clouds are more likely to occur in the northern hemisphere, otherwise as region B (Mao et al., 2019).

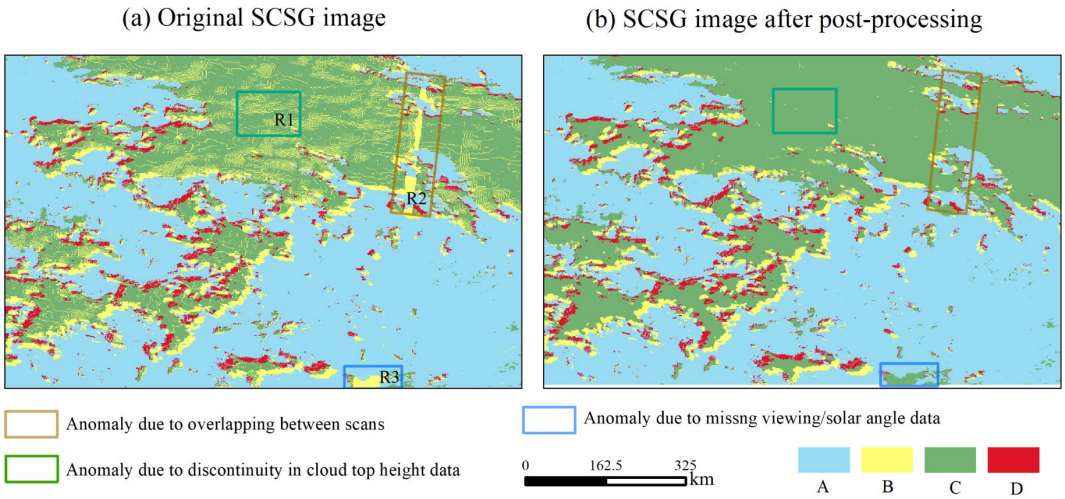

Fig. 3 An example of SCSG partition based on the 18th daytime MODIS/Aqua LST image in 2003 over a subregion of Qinghai-Tibet Plateau (QTP) (a) before and (b) after anomaly removal. The SCSG regions (A-D) are shown in different colors, and three subregions (R1, R2, and R3) with typical anomaly sources are marked by rectangles.

2.3. Bias correction of cloudy-sky LST values in region D

SCSG region D was in the shadow of clouds but could be viewed from the satellite owing to the differences between the solar illumination angles and satellite observation angles. The known LST values in region D served as independent cloud-affected observations to be used to formulate a relationship to account for cloud-induced biases so that missing LST values in region C due to cloud cover could be determined. The LST values of region D pixels could also be biased, because in the MODIS LST inversion algorithm, the band emissivities retrieved on previous days were used as the initial emissivity values for new retrievals. In the presence of clouds, the retrieved TIR band emissivity values may be lower than normal values under cloudy conditions (Wan 2008). Therefore, a procedure at the fundamental level of the LST inversion algorithm is needed to correct for the LST biases in region D pixels and needs to be tested prior to becoming qualified for use in subsequent

steps. However, in this study, this task was accomplished based on *in-situ* LST observations at ground sites representative of LST variations in the vicinity and performed independently of the proposed approach.

For a model to be built to treat biases for region D pixels, valid data points were located from the LST time-series observations at representative ground sites. The SCSG regions were created for all MODIS LST images spanning multiple years. For each MODIS cell with a representative site, the timing at which the cell was classified as region D was determined and used as the basis for finding the corresponding *in-situ* data points. It was likely that no exact temporal match existed between the satellite and *in-situ* observations as the former was instantaneous, whereas the latter was often measured hourly. We linearly interpolated the *in-situ* data at the satellite overpass time from the two closest time points. For example, the *in-situ* data points between 1:00 and 2:00 pm local time were linearly interpolated to provide the *in-situ* LST for a satellite acquisition time of approximately 1:30 pm for MODIS/Aqua. It should be noted that the fraction of usable data points for QTP may not be large due to the small size of region D and the limited number of representative QTP sites. Based on the valid data pairs comprising the SCSG region-D LST and simultaneous *in-situ* cloudy-sky LST, empirical mathematical models were constructed to remove systematic biases from the region D LST values. In the case study of QTP, the linear model was found to be satisfactory for this purpose (see Section 4.3).

2.4. Estimation of clear-sky LST equivalents

For SCSG regions B, C, and D, the clear-sky LST equivalents were interpolated. This study adopted the approach developed by Chen et al. (2021), based on the concept of similarity, under the

assumption that each interpolated LST pixel had spatially similar pixels in terms of temperature change over time. This approach depended on the reference LST images that were not only temporally adjacent to the image being interpolated, but also had a matching overpass time and spatial coverage. For each missing pixel in the interpolated image, temporally proximate images, such as those within a time window (e.g., 15 d) centered on the interpolated image, were considered the reference images only if the images had a valid LST value at the interpolated location and contained a relatively high proportion of valid pixels. Consequently, the reference images were variable for each interpolated pixel.

With each reference image pertinent to the interpolated pixel, the pixel value was estimated from the empirical orthogonal function (DINEOF) method (Alvera-Azcárate et al., 2005; Beckers and Rixen 2003). This method relied on the LST values of similar pixels determined from both the interpolated image and each associated reference image based on a high consensus on a number of environmental predictors, such as normalized difference vegetation index (NDVI), digital elevation model (DEM), slope, aspect, and clear-sky direct shortwave solar radiation. Multiple LST estimates could be made for each interpolated pixel because a given interpolated pixel could be associated with multiple reference images. A Bayesian approach (Kumar et al., 2007) was then applied to merge these initial estimates and obtain the best estimate of LST for the interpolated pixel. It should be noted that it was likely that some pixels had no qualified reference images in which case these pixels were assigned null. According to our experiments, the fraction of pixels with null values for each image after the interpolation was small. Some conventional geostatistical interpolation approaches can be employed to effectively fill the remaining missing pixels, given the small number, and produce a non-missing LST image.

This approach was tested with purposively generated large data gaps in the MODIS LST images of QTP and was used to compare the interpolation results to the actual data. As a result, it was found to outperform the conventional approaches in terms of interpolating for large areas of missing data. As this approach used only clear-sky LST values, the interpolation results did not include cloud effects.

2.5. Recovery of missing cloudy-sky LST values in region C

The pixels in region D with bias-corrected cloudy-sky LST values provided important information about cloud effects on LST in order to recover missing LST values in region C due to cloudiness. Although the SCSG effect is only based on cloud shape, the LST values in region D were synthesized from all cloud effects, such as cloud shape, thickness, and composition, and were then strengthened via the bias correction process based on the *in-situ* observations of cloudy-sky LST. In the recovery of missing cloudy-sky LST values in region C, it was assumed that, for each interpolated pixel in region C, there were spatially similar pixels in region D with respect to the environmental predictors and clear-sky LST equivalents. The interpolated pixels and their similar pixels had similar cloud conditions and shared a statistical model representing the cloudy-sky LST value as a function of the environmental predictors. Thus, for each interpolated pixel, a statistical model could be identified from similar pixels. In our implementation, interpolation was conducted on the clusters instead of pixels for computational efficiency. The steps involved spatially clustering the pixels in region C, identifying pixels in region D with high similarity to the cluster centroid, training a specific LST-prediction model for each cluster, and then applying the model to estimate unknown LSTs of region C pixels that were part of that cluster. The same steps were iterated for all

clusters in region C.

To perform a cluster analysis between pixels and identify similar pixels, the environmental predictors should be determined. LST is the result of many combined impacts and is closely related to a number of environmental factors, such as land-use/cover change, NDVI, soil moisture, elevation, slope, aspect, and incident solar radiation (Deng et al., 2018; Tian et al., 2012; Van De Kerchove et al., 2013). Incident solar radiation partially reflects cloud characteristics (Kasten and Czeplak 1980) and helps to find pixels under similar cloud conditions. In this study, the attributes specified for cluster analysis were clear-sky LST equivalents; topographic factors of elevation, aspect, and slope; surface condition factors of NDVI and albedo; and solar radiation factors of downward shortwave radiation (DSR) and net surface shortwave radiation (NSSR). These data were obtained from MODIS, DEM, and DEM-derived datasets. The k-means method was applied with 1000 clusters. The centroids of all the clusters were identified. The same set of attributes for cluster analysis was used to define similar pixels in region D. A simple Euclidean distance equation was used as the similarity function. For each cluster centroid in region C, the first 1000 pixels with the highest similarities formed a similar group for the cluster centroid.

The MARS model was used to build a prediction model for cloudy-sky LST, given its advantage in handling nonlinear dependencies and high-dimensional data. The MARS algorithm takes the form of an expansion in the product spline basis functions, where the number of basis functions and the parameters associated with each function are automatically determined by the training data. This procedure is motivated by recursive partitioning and shares the ability to capture high-order interactions. This model has a forward process for generating a set of basis functions over the domain of interest and a backward process for preventing overfitting. To estimate cloudy

LST, one MARS model was trained for each cluster in region C as a function of the environmental predictors and the clear-sky LST equivalent (Eq. (3)). The well-trained MARS models were then applied to the pixels in region C on a cluster-by-cluster basis to estimate their cloudy-sky LSTs.

$$LST_{cld} = f_{MARS}(S^D, LST_{clr}) \tag{3}$$

where LST_{cld} is the cloudy-sky LST value; LST_{clr} is the clear-sky LST equivalent; and S^D represents the environmental predictors of elevation, aspect, slope, NDVI, albedo, DSR, and NSSR.

3. Study area and performance evaluation

3.1. Study area and data

The proposed approach was tested on the study area of Qinghai-Tibet Plateau (Fig. 4). The plateau is bounded by 26º00′–39º47′N and 73º19′–104º47′E, with an average elevation of more than 4000 m above sea level (a.s.l.) and an area of approximately 2.6 million km^2. Due to the combined effect of westerlies, the East Asia monsoon, and the Tibetan Plateau monsoon, there were significant cloud-related data gaps in the MODIS LST data products, typically extending more than half a year (Yu et al., 2015). The experimental satellite daytime LST data were obtained from the MODIS Land Surface Temperature/Emissivity Daily L3 Global 1 km dataset (MYD11A1) onboard the Aqua satellite with equatorial overpasses at approximately 1:30 pm in ascending orbit and 1:30 am in descending orbit. To align with the *in-situ* measurements used in this study, data for 2002–2004 and 2009–2010 were selected.

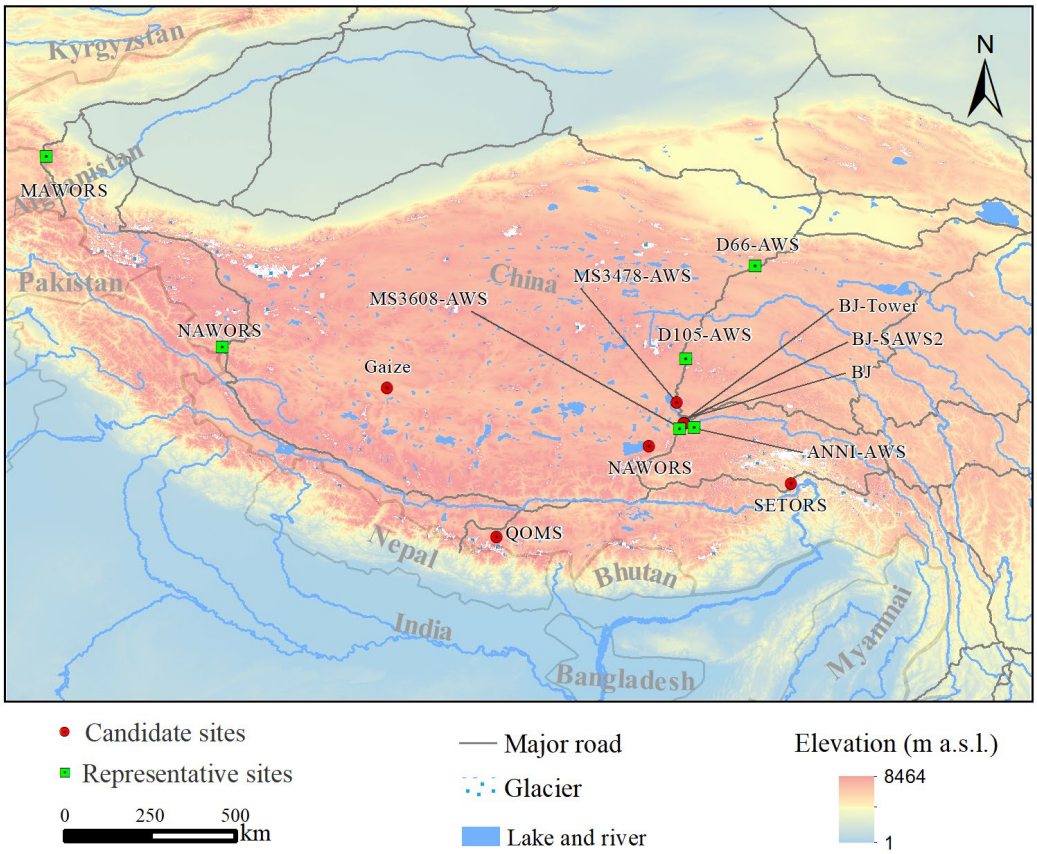

Fig. 4 Map showing the topography of Qinghai-Tibet Plateau and the locations of candidate sites where *in-situ* LST observations were available. Representative sites were determined from the candidate sites with reference to their representativeness for the 1-km MODIS LST pixels that contained the *in-situ* measurement sites.

The two MODIS products of the Geolocation Fields 5-Min L1A Swath 1 km dataset (MYD03), which provides solar and satellite observation angles, and the Clouds 5-Min L2 Swath 1 km dataset (MYD06_L2), which provides cloud-top heights, were used to support the SCSG partitioning. The data used to estimate clear-sky LST equivalents were the Vegetation Indices 16-Day L3 Global 1 km dataset (MYD13A2), the Shuttle Radar Topography Mission (SRTM) 90 m DEM, and DEM-derived data, such as slope and aspect. The clear-sky direct shortwave solar radiation data were estimated from the incident angle as a function of the time of year, latitude, altitude, slope, and

aspect, as were diffuse and reflective radiation (Kumar et al., 1997).

The environmental predictors supporting cloudy-sky LST retrieval were extracted from the following MODIS data family: MYD13A2 NDVI, the Surface Radiation Daily/3-Hour L3 Global 1 km dataset (MCD18A1), Global Land Surface Satellite (GLASS) albedo data (Liang et al., 2013), and SRTM providing topographic factors. MCD18A1 provides a 1-km gridded MODIS Terra/Aqua combined DSR at two temporal resolutions (instantaneous and 3-h). Because the instantaneous DSR data at the time of the MODIS overpass contain significant coverage gaps due to cloud contamination, we used the 3-h DSR data and interpolated the value at the overpass time from the two closest time points. GLASS albedo data were also used (Liang et al., 2013), because they offer gap-free, high-quality albedo data for this study. The NSSR, defined as NSSR = DSR × (1-albedo), was calculated based on MCD18A1 and the GLASS albedo data. The 90-m SRTM DEM data were up-scaled by computing an 11 × 11 aggregate mean before bilinear resampling to align with the 1-km MODIS pixel centers.

Two all-weather LST datasets publicly available from the National Tibetan Plateau Data Center were used to cross-validate the interpolated cloudy-sky results of this study. One was a fused 1-km LST dataset from the Advanced Microwave Scanning Radiometer 2 (AMSR2) and MODIS/Aqua daytime/nighttime LST (MYD11A1) data (hereafter referred to as PTM LST) spanning 2000–2020 using a cumulative distribution function-matching approach and a multiresolution Kalman-filtering approach (Xu and Cheng 2021). The other was a merged 1-km LST dataset generated by merging the MYD11A1/LST daytime/nighttime product and GLDAS LST data (hereafter referred to as RTM LST) spanning 2000–2020 based on a temporal component-decomposition model, which decomposed cloudy LST time series into the three components of an annual cycle, a diurnal change,

and cloud effect, with the annual and diurnal components being estimated from clear-sky LSTs and with the cloud effect component from reanalysis data (Zhang et al., 2021). A subset of 2002–2004 and 2009–2010 was extracted from the two datasets for a comparison to our interpolated results.

Although many datasets were required as the inputs to the proposed approach, they could be acquired from the same MODIS product family (Table 1). The only exception was the SRTM data, which were assumed to be constant over the study period. Based on the literature review, the accuracies of all the satellite data collected for QTP are listed in Table 1. Because the MYD03 product only provides satellite viewing angles and solar illumination angles, no accuracy was provided. The same MODIS family was used to collect data in order to maximize data availability and minimize uncertainties associated with spatiotemporal scale mismatches.

Table 1 Datasets as the inputs to the proposed approach and their reported accuracies over QTP based on literature review. Other variables required were derived from these datasets. The Shuttle Radar Topography Mission (SRTM) data were up-scaled to 1 km to match the other data. RMSE: root mean square error; MAE: mean absolute error; and STD: standard deviation.

Product code	Spatial/temporal resolutions	Variable(s) provided	Accuracy over QTP
MYD11A1	1 km/daily	Daytime LST	3.34–5.58 °C in RMSE (Duan et al., 2019)
		View time	/
MYD03	1 km/daily	View zenith/azimuth angle	/
		Solar zenith/azimuth angle	/
MYD06_L2	1 km/5 min	Cloud-top height	0.87–1.58 km in MAE (Yang et al., 2021)

MYD13A2	1 km/16 d	NDVI	0.042–0.086 in RMSE (Sajadi et al., 2021)
MCD18A1	1 km/3 h	Downward shortwave radiation	134.8–172.6 W/m^2 in RMSE (Wang et al., 2021)
GLASS Albedo	1 km/8 d	Albedo	Black-sky: 0.055–0.092; white-sky: 0.052–0.088 (RMSE) (An et al., 2020)
SRTM	90 m	Elevation	4.58 ± 26.01 m in STD (Huang et al., 2011)

3.2. Representative sites and performance of clear-sky MODIS LST for QTP

Only a few sites in QTP provided *in-situ* LST observations. We collected *in-situ* observations from a total of 14 candidate sites (Fig. 4), mainly from the following two sources: the Coordinated Energy and Water Cycle Observations Project (CEOP) for eight sites with a data period of 2002–2004 (Ma et al., 2006) and the Institute of Tibetan Plateau Research (ITP) of the Chinese Academy of Science for six sites for hourly data as of 2005 (Ma et al., 2020). Only observations for the period of 2009–2010 at the ITP sites were used since one of the ITP sites became operational in 2009.

Unlike the CEOP dataset, which provides ready-to-use LST data, the ITP dataset contained only measurements of outgoing and incoming shortwave and longwave radiation fluxes, which were used to derive LST from the Boltzmann's law thus:

$$LST_g = \left[\frac{R_g - (1-\varepsilon_b)R_d}{\sigma\varepsilon_b}\right]^{1/4} \quad (4)$$

where LST_g is the *in-situ* LST; R_g is the upwelling broadband hemispherical radiance (W/m^2); R_d is

the downwelling broadband hemispherical radiance (W/m^2); σ is the Stefan-Boltzmann constant (5.67×10^{-8} W/m^2/K^4); and ε_b is the broadband emissivity, which can be estimated from the Advanced Space Thermal Emission and Reflection Radiometer (ASTER) Terra emissivity product (AST_08 v003) via a spectral-to-broadband linear regression equation as follows (Cheng et al., 2013):

$$\varepsilon_{\mathrm{b}} = 0.197 + 0.025\varepsilon_{10} + 0.057\varepsilon_{11} + 0.237\varepsilon_{12} + 0.333\varepsilon_{13} + 0.146\varepsilon_{14} \quad (5)$$

where ε_{10}-ε_{14} are the narrowband surface emissivities of ASTER bands 10–14, respectively.

In this study, we identified representative sites from the 14 candidate sites from two perspectives. First, we measured the spatial homogeneity of the sites from the spatial standard deviation (STD) values of LSTs based on ASTER LST data (AST_05 v003) at a spatial resolution of 90 m, as described by Duan et al. (2019). More specifically, a single MODIS LST pixel covering 11 × 11 ASTER pixels and the LST observations on the ASTER pixels were used to calculate the spatial STD values for the ground site of interest. A multi-year average of the spatial STD values can indicate site representativeness within the corresponding MODIS cell in terms of spatial homogeneity. Second, we measured site representativeness based on the bias metrics between the *in-situ* clear-sky LST measurements and the corresponding MODIS LSTs in SCSG region A.

In our quantitative evaluation, the following performance metrics were used: bias (BIAS), mean absolute error (MAE), root mean square error (RMSE), unbiased RMSE (ubRMSE), and coefficient of determination (R^2). We used BIAS for average error and MAE for average absolute error. Unlike BIAS and MAE, RMSE quantifies the errors with more weights for large deviations, whereas ubRMSE excludes systematic errors from RMSE. R^2 measures the agreement between the *in-situ* measurements and interpolation results, calculated as the proportion of the variation in the response variable that is predictable from the explanatory variables. Higher values of R^2 and lower

values of BIAS, MAE, RMSE, and ubRMSE indicate better performance. A negative R^2 value indicates that the predictions are worse than a constant function that always predicts the mean of the data.

Fig. 5 shows the representativeness of the sites in terms of the spatial homogeneity of LST, as measured by the spatial STD values of LSTs over the 1-km MODIS pixels containing the sites based on the ASTER LST observations for 2002–2010. Among the 14 candidate sites, the CEOP sites, such as BJ-SAWS2 (C2), BJ-Tower (C3), and MS3478 (C7) (Fig. 5a), and the ITP sites, such as BJ (ITP1), QOMS (ITP5), and SETORS (ITP6) (Fig. 5b), showed significant heterogeneity with a high median or a wide range of the spatial STD values. When the MODIS/Aqua clear-sky daytime LST observations were compared to the *in-situ* LST measurements available at the MODIS acquisition time (Fig. 6), the sites of MS3478-AWS (C7), BJ (ITP1), QOMS (ITP5), and SETORS (ITP6) showed considerable biases in RMSE, MAE, and BIAS. For these sites, the LST heterogeneity was also observed in terms of the spatial STD values. However, for some sites, such as Gaize (C6) and NAMORS (ITP4), identified as relatively homogeneous in terms of the spatial STD values, the RMSE values between the *in-situ* LSTs and MODIS LSTs differed by more than 5 °C under clear skies. While Gaize (C6), BJ (ITP1), NAMORS (ITP4), and SETORS (ITP6) showed a large BIAS range of -9.62 to -4.14 ºC, their ubRMSE values were less than 3.5 °C, indicating that the satellite clear-sky LST observations at these locations were largely subject to systematic biases.

With the criteria of less than 3.5 ºC in the median spatial STD, less than 4.5 ºC in RMSE, and less than 2.5 ºC in BIAS between the *in-situ* LSTs and MODIS clear-sky LSTs, the four CEOP sites of ANNI-AWS (C1), D105-AWS (C4), D66-AWS (C5), and MS3608-AWS (C8) and the two ITP sites of MAWORS (ITP2) and NADORS (ITP3) were determined as the representative sites of a 1-

km MODIS pixel for the LST variations (Table 2).

Prior to evaluating the performance of the interpolated cloudy-sky results, we tested the performance of MODIS/Aqua clear-sky daytime LST data at the six representative QTP sites in order to obtain the baseline accuracy for the proposed approach. The overall performance of the MODIS/Aqua clear-sky daytime LST observations was excellent for QTP, with a low MAE value of 2.66 ºC, a low systematic BIAS value of 0.06 ºC, and a high R^2 value of 0.86 (n = 1078). Typically, MODIS LST data were reported to exhibit relatively low consistency with the *in-situ* observations for QTP than for flat regions due to the complexity of the mountainous terrain (Duan et al., 2019; Ryu et al., 2008), a factor that significantly limited the site representativeness in the MODIS pixel. It should be noted that we only evaluated sites based on MODIS/Aqua daytime LST data. Since the spatial variability of nighttime LST is usually less than that of daytime LST (Duan et al., 2019), there may be more sites representative of a MODIS pixel for nighttime LST.

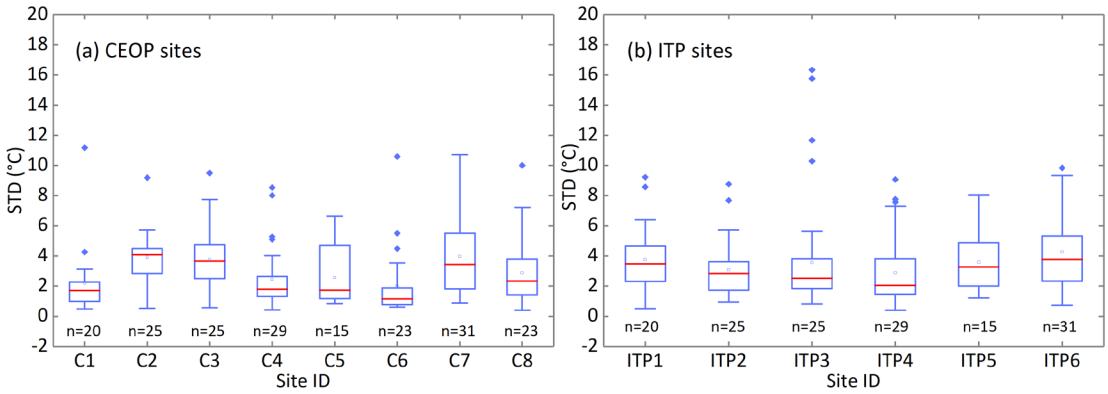

Fig. 5 Spatial homogeneity of available LST sites for QTP, as measured by the STD values of LSTs in a 1-km MODIS pixel containing the *in-situ* measurement site, based on LST observations from 11 × 11 Advanced Space Thermal Emission and Reflection Radiometer (ASTER) LST pixels covered by this MODIS pixel. (a) shows the boxplot of the spatial STD values for the Coordinated Energy and Water Cycle Observations Project (CEOP) network sites: C1(ANNI-AWS), C2(BJ-SAWS2), C3(BJ-Tower),

C4(D105-AWS), C5(D66-AWS), C6(Gaize), C7(MS3478-AWS), and C8(MS3608-AWS). (b) shows the boxplot of the spatial STD values for the monitoring sites operated by Institute of Tibetan Plateau Research (ITP) of Chinese Academy of Science: ITP1(BJ), ITP2(MAWORS), ITP3(NADORS), ITP4(NAMORS), ITP5(QOMS), and ITP6(SETORS). *n* is the number of valid samples for 2002–2010 used to create the boxplot. The boxes represent 25%–75% quartiles and the whiskers are 1.5 interquartile ranges from the medians shown as the red lines in the boxes. The dots denote outlier values. The site locations can be found in Fig. 4.

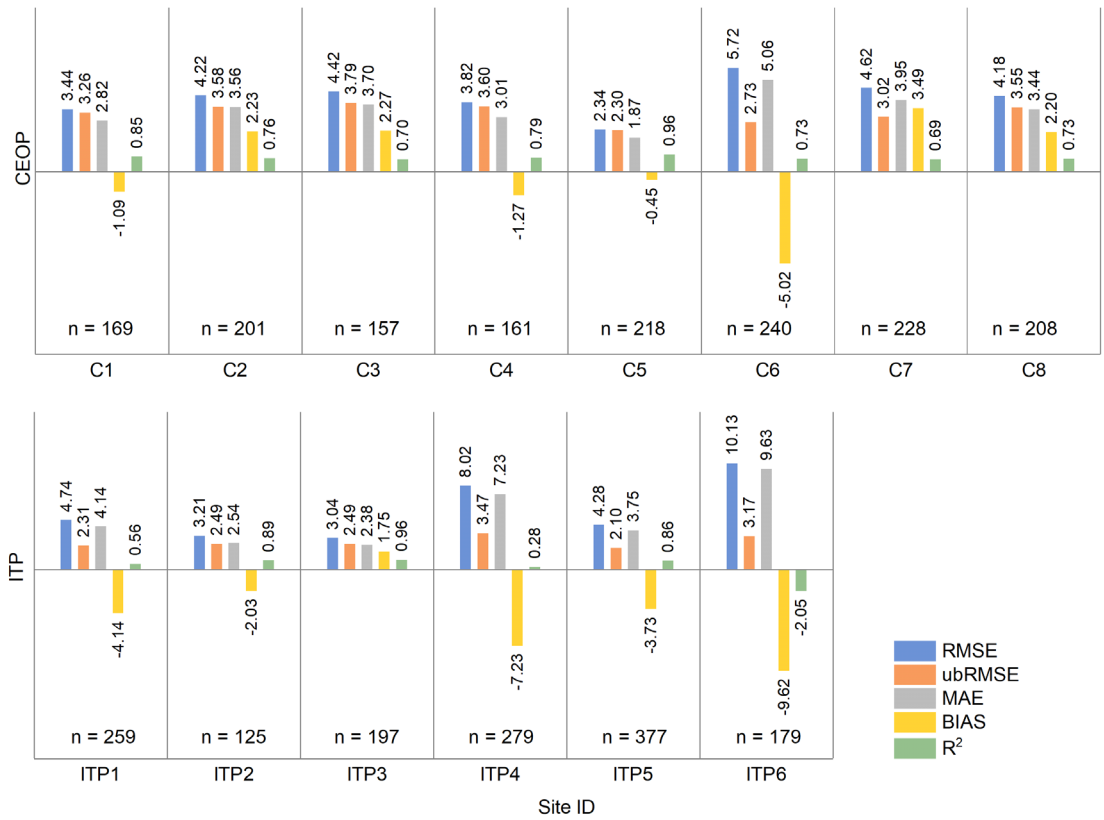

Fig. 6 Performance of MODIS/Aqua clear-sky LST observations at candidate sites, as indicated in a variety of metrics. ubRMSE: unbiased RMSE; R^2: coefficient of determination. The negative R^2 value found at ITP6 indicates that the MODIS clear-sky LST is a worse fit than the mean of corresponding *in-situ* values. The same site codes are applied as in Fig. 5.

Table 2 Six QTP sites identified as the representative sites from the candidates consisting of the CEOP network sites and the ITP monitoring sites. These sites were used to calibrate the cloudy-sky LST values in region D and validate the interpolated results in region C.

Station	Source	Latitude (ºN)	Longitude (ºE)	Elevation (m a.s.l.)	Land cover	Data length
ANNI-AWS	CEOP	31.25	92.17	4480	Bare land	2002–2004
D66-AWS	CEOP	35.52	93.78	4585	Bare land	2002–2004
D105-AWS	CEOP	33.06	91.94	5039	Bare land	2002–2004
MS3608-AWS	CEOP	31.23	91.78	4589	Bare land	2002–2004
NADORS	ITP	33.39	79.79	4270	Alpine desert	2009–2016
MAWORS	ITP	38.41	75.05	3668	Alpine desert	2010–2016

3.3. Strategies for evaluating the interpolation results

The *in-situ* observations at the representative sites served to correct the cloudy LST values in region D and validate the interpolated results in region C. We evaluated the proposed approach based on two aspects. First, we extracted the time series of the interpolated cloudy-sky LST values at the sites of MODIS pixels and compared them to the corresponding *in-situ* measurements. The *in-situ* cloudy LST measurements corresponding to SCSG region D were used for bias correction, while those corresponding to region C remained unused so that they could be used as validation data.

Second, we compared the interpolated MODIS/Aqua LST images for 2002–2004 and 2009–2010 with images from the two all-weather LST datasets of RTM LST (Zhang et al., 2021) and PTM LST (Xu and Cheng, 2021) for the same dates. We visually inspected these images for seasonal LST

characteristics at the regional scale and spatial patterns in typical subregions. We also evaluated the two LST datasets against the *in-situ* cloudy-sky observations at the representative QTP sites via the aforementioned quantitative metrics. Data points falling outside the 95% quantile were considered outliers and excluded prior to analysis.

4. Results

4.1. Partitioning of the MODIS LST images in relation to SCSG effect

We arbitrarily selected four MODIS/Aqua daytime LST images (the 92nd, 213th, 305th, and 348th day of 2010), each representing a different season in 2010, to demonstrate the partitioning results based on the SCSG effect (Fig. 7). The original MODIS LST images and the resultant SCSG partitions are shown in columns 1 and 2 in Fig. 7, respectively. The partitioned SCSG regions fulfilled our expectations, with regions B and D being mainly distributed along the edges of cloud cover and with regions A and C showing actual clear and actual cloudy sky areas, respectively. To verify these SCSG-based results, we visually inspected the partitioned SCSG regions on the MODIS false-color composite images via the same approach used in a previous study (Wang et al., 2019). Despite the satisfactory partitioning, some small problematic stripes even after post-processing measures were detected in some of the SCSG-partitioned images when large-scale overlaps occurred between the adjacent MODIS scans, such as the anomalous yellow stripes appearing on the images of the 92nd and 305th days east of QTP in Fig. 7.

Fig. 8 shows the statistics of the percentage of pixels in the four SCSG regions for QTP in 2010. Fig. 8a shows the daily percentage distribution of pixels by region type, while Fig. 8b shows the number of pixels in region D for each day. Overall, regions A (with known clear-sky LST values)

and C (with unknown cloudy-sky LST values) occupied most of the area in each SCSG image. Regions B (with unknown clear-sky LST values) and D (with known cloudy-sky LST values) accounted for a relatively small proportion of the total pixels for QTP (0.4–7.8% and 0.5–7.9%, respectively, based on the daily MODIS/Aqua daytime LST images). The majority of cloudy pixels fell within region C, where interpolation was expected to be applied. Because QTP contained approximately 2.6 million pixels at a 1-km resolution, the absolute number of pixels in region D still remained large (Fig. 8b). In 2010, the number of region D pixels in each SCSG image ranged from 14,761 to 220,991 with a median of 116,984, and these pixels were scattered throughout the study area. The large number of pixels in region D ensured that there were enough samples to represent the complex effects of cloudy skies on LST.

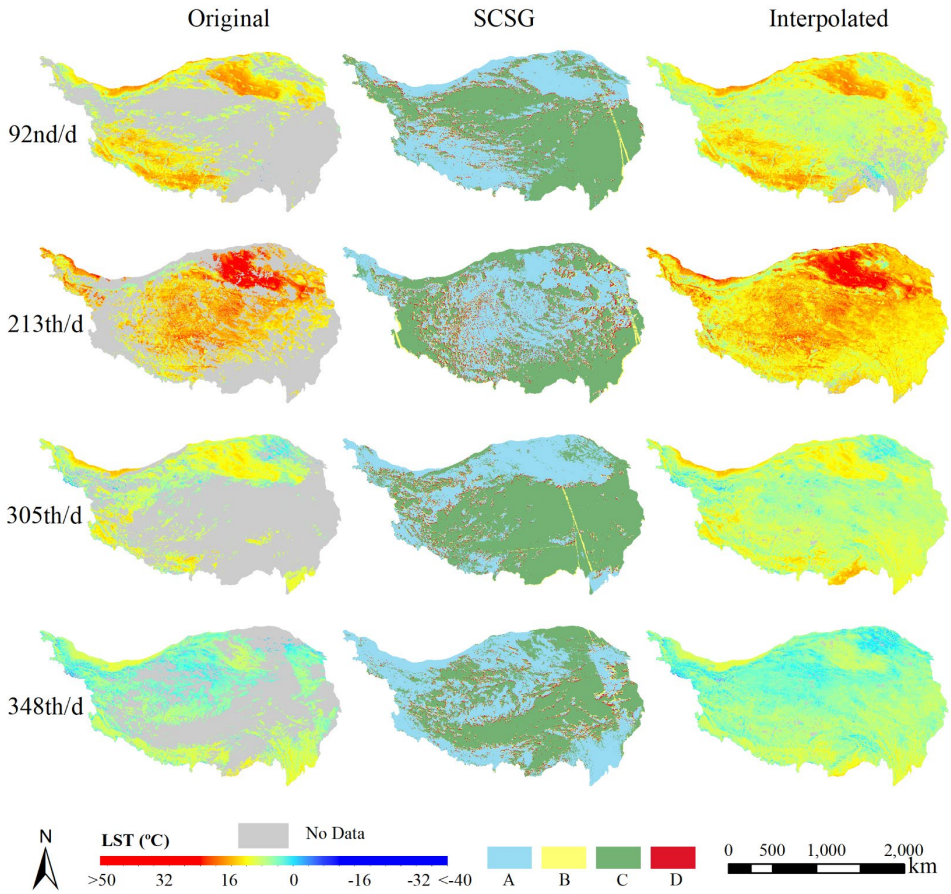

Fig. 7 Maps showing (a) the MODIS/Aqua daytime LST images, (b) the corresponding SCSG-

partitioned images, and (c) the interpolated results of this study on four arbitrarily chosen dates (the 92nd, 213th, 305th, and 348th day of 2010), with one from each season in 2010 for QTP. d: daytime.

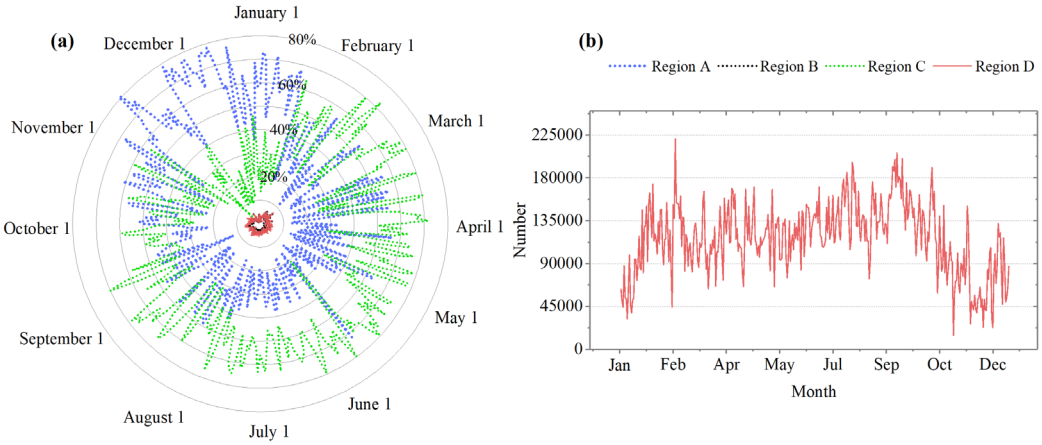

Fig. 8 Statistics on the percentage of pixels in the four regions (A, B, C, and D) in the SCSG-partitioned images resulting from MODIS/Aqua daytime LST images in 2010. (a) Rose plot showing daily percentage distribution of pixels by region type. The black dotted lines for region B are mostly buried by the red solid lines. (b) Numbers of pixels in region D (with known cloudy-sky LST values) for each day in 2010.

4.2. Performance of bias-corrected cloudy-sky MODIS LST values in region D

Based on the six identified representative sites, we found 164 valid LST data pairs comprising the region D LST values of MODIS/Aqua and the corresponding *in-situ* cloudy-sky LST values for 2002–2004 at the CEOP sites and for 2009–2010 at the ITP sites (Fig. 9). As can be seen in Fig. 9a, the region D LST values presented a pronounced negative deviation from the *in-situ* cloudy-sky measurements (BIAS = -4.48 ^{o}C). Similar negative biases were previously reported for the MODIS Terra/Aqua cloudy-sky LST pixels (Østby et al., 2014; Williamson et al., 2013; Zhang et al., 2016). The negative discrepancies were largely related to the questionable estimates of the MODIS TIR

band emissivities under cloudy conditions. At the representative QTP sites, we found that the MODIS/Aqua daytime cloudy-sky LSTs were highly correlated with the *in-situ* measurements, with a Pearson's correlation coefficient (R) of 0.92 and with no apparent site dependency, which we examined for each individual site. After a linear model was applied to remove systematic biases from the original MODIS/Aqua daytime cloudy-sky LST values, the bias-corrected data points (Fig. 9b) appeared more concentrated along the diagonal line. The systematic biases (BIAS) in the corrected satellite cloudy-sky LSTs underwent a substantial reduction (before correction: -4.48 ºC; after correction: -0.09 ºC). In parallel, the MAE value declined from 4.98 to 3.58 ºC, while the R^2 value increased from 0.67 to 0.70. All these metrics consistently indicated the usability of bias-corrected region D pixels in providing the samples of actual cloudy-sky LST values.

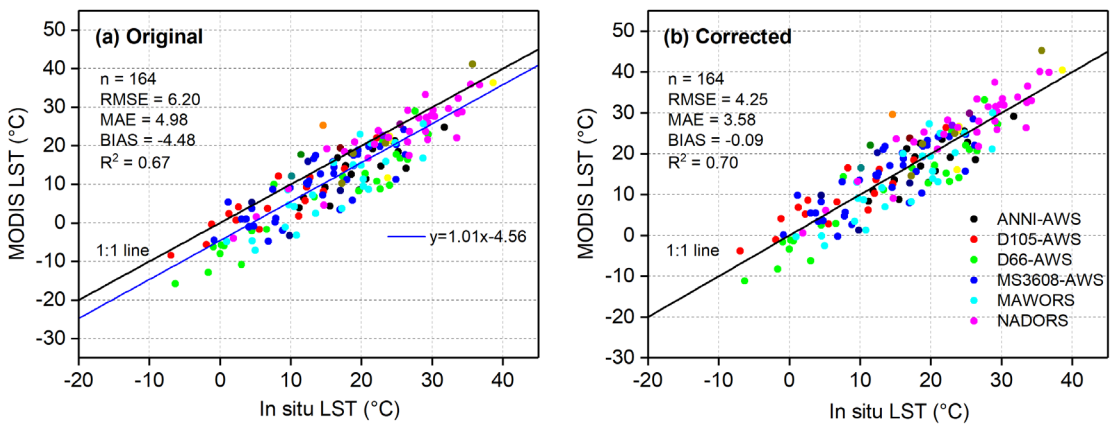

Fig. 9 Bias-corrected MODIS/Aqua daytime LST values of the SCSG region D pixels, showing significantly improved agreement with the *in-situ* cloudy-sky LST observations at the six representative QTP sites, compared to values before correction. (a) Before bias correction. (b) After bias correction. Data points were extracted for 2002–2004 at the CEOP sites and for 2009–2010 at the ITP sites when the site locations were classified as region D due to the SCSG effect.

4.3. Accuracy assessment of the interpolated cloudy-sky LST pixels

The interpolated results of this study are shown in the right-hand column of Fig. 7. The fractions of the missing data in the four MODIS/Aqua LST images (the 1st column in Fig. 7) were 59% in spring, 51% in summer, 65% in autumn, and 50% in winter. The interpolated results well represented the spatial details of LST over QTP and showed a natural textural transition over the data-gap regions without significant anomalies. In terms of the spatial completeness, the proposed approach successfully interpolated most of the missing pixels over QTP but left a small number of pixels uninterpolated (e.g., southern QTP on day 92 in 2010). The remaining missing pixels in the four interpolated LST images for 2010 were 10.75% in spring, 2.45% in summer, 1.74% in autumn, and 2.00% in winter. This was because the proposed approach interpolated the clear-sky LST equivalents based on the multiple proximate reference images determined from a 15-d window centered on the interpolated image. Thus, pixels for which the LST values were missing in both the interpolated and reference images may not be interpolated. These small data gaps can be effectively filled by using the conventional geostatistical methods.

Validation was conducted by using the *in-situ* cloudy-sky LST observations for 2002–2004 at the four CEOP sites and for 2009–2010 at the two ITP sites (Fig. 10). Overall, the interpolated results agreed well with the *in-situ* observations, and the data points were concentrated along the 1:1 line at all the six representative sites. The goodness-of-fit (R^2) value between the interpolated LSTs and *in-situ* cloudy-sky LSTs varied between 0.59 and 0.81 across all the sites, while the RMSE values varied between 4.33 and 5.39 ºC, both indicating good interpolation accuracy. Except for D66-AWS (Fig. 10c) and MS3608-AWS (Fig. 10d), the ubRMSE values were close to the RMSE values at most sites, indicating minimal systematic errors after the interpolation. Since this approach

mostly relied on the MODIS data products, the clear-sky MODIS LST performance for QTP provides the best possible accuracy that this approach can achieve for the cloudy-sky LST interpolation. Table 3 shows the performance of the clear-sky MODIS/Aqua LST data for QTP as well as that of our interpolated cloudy-sky results for the same representative sites. The interpolated cloudy-sky LSTs in SCSG region C were slightly biased with a BIAS value of 2.11 ºC, higher than the BIAS value of 0.06 ºC under clear skies. The increases in RMSE (from 3.32 to 4.83 ºC) and MAE (from 2.66 to 3.99 ºC) and a decrease in R^2 (from 0.86 to 0.74) also indicated slightly lower performance for the interpolated cloudy-sky LST than for the clear-sky MODIS LST observations. The modest degradation in accuracy was ascribed to the use of the cloudy-sky LST samples, that is, the bias-corrected LSTs in SCSG region D, which performed slightly worse than their clear-sky counterparts with an MAE value of 3.58 ºC and an R^2 value of 0.70 (Fig. 9b), as well as to the uncertainties introduced by the proposed approach.

To better understand the performance of the interpolation, we compared the interpolation results to the *in-situ* measurements at the six representative sites from the perspective of time series (containing all-weather LSTs under both clear and cloudy skies) (Fig. 11). Overall, the interpolated time series of this study showed high temporal consistency with the *in-situ* measurements, and the interpolated time series successfully reproduced seasonal variations in LST at the six sites (Fig. 11). In particular, the interpolated LSTs showed close agreement with the *in-situ* cloudy-sky observations at many time intervals, such as 1 August to 27 December 2004 at D66-AWS (Fig. 11c), 11 August to 31 December 2010 at MAWORS (Fig. 11e), and 21 October to 28 December 2010 at NADORS (Fig. 11f). We also observed some discrepancies in the interpolated time series, as shown in Fig. 11. For example, an overestimation in the interpolated cloudy-sky LSTs from 1 March to 29 May 2004

at D66-AWS (Fig. 11c) and an underestimation from 17 June to 27 July 2010 at MAWORS occurred (Fig. 11e). The MODIS clear-sky LSTs showed similar positive and negative discrepancies from the *in-situ* observations for the same time intervals. Therefore, the discrepancies observed in the interpolated cloudy-sky LSTs were probably due to errors inherent in the MODIS clear-sky LST data rather than the deficiency of the interpolation approach. There were a small number of data gaps, such as 28 November 2002 to 3 January 2003 at ANNI-AWS (Fig. 11a) and 14 December 2002 to 1 January 2003 at D66-AWS (Fig. 11c). These data gaps were caused by the missing *in-situ* LST data or missing interpolated results due to the failure to locate valid reference images during the interpolation of clear-sky LST equivalents.

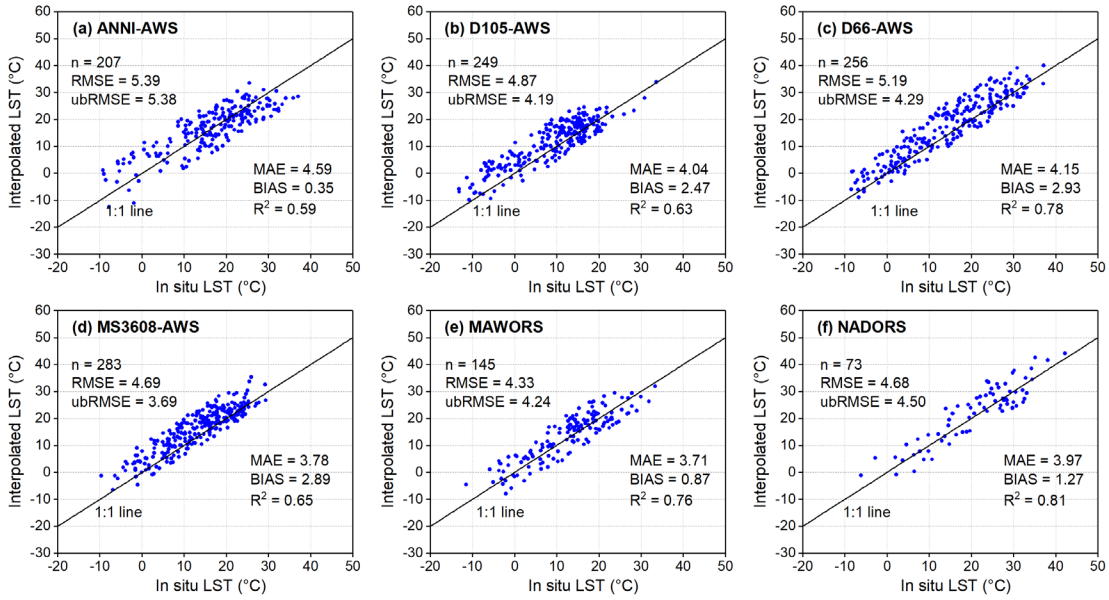

Fig. 10 Scatter plots showing interpolated cloudy-sky LST values and the corresponding *in-situ* cloudy-sky LST measurements at the representative LST sites of QTP. The related interpolated pixels were in region C when the SCSG effect was considered.

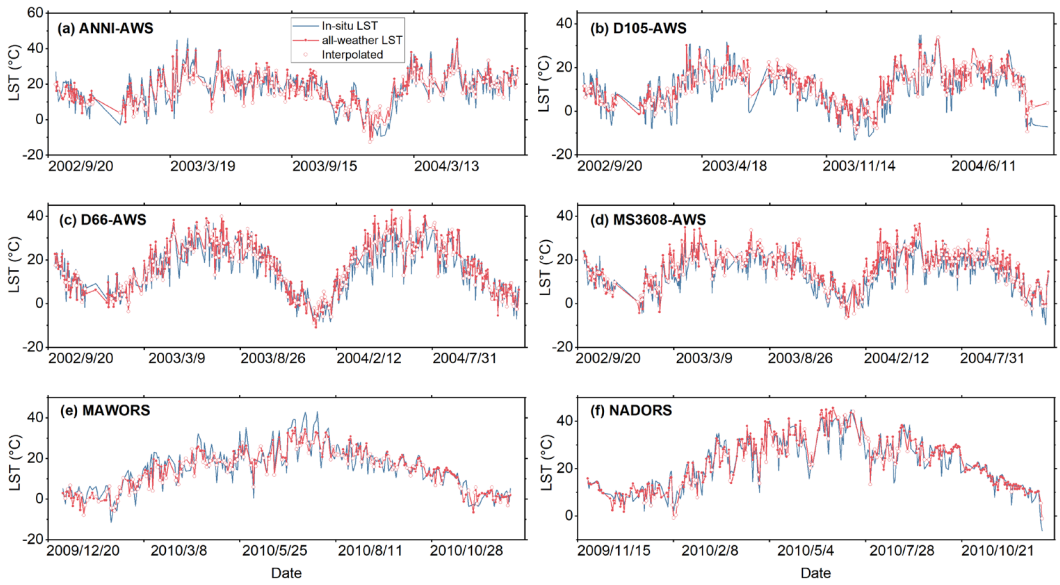

Fig. 11 Time series of the all-weather MODIS/Aqua daytime LST values and the corresponding *in-situ* LST measurements at the representative QTP sites. The hollow circles indicate interpolated cloudy-sky LST values, whereas the solid red dots show clear-sky LST observations. Note that data length varied by site, and some data gaps (shown as long straight lines) existed due to missing *in-situ* observations or interpolated results.

Table 3 Accuracy of the interpolated daytime cloudy-sky results at the representative QTP LST sites as well as the MODIS/Aqua daytime clear-sky LST data at the same sites used as the reference for comparison. The metrics were calculated based on data aggregated from all the six representative sites.

Weather condition	*n*	RMSE (ºC)	MAE (ºC)	BIAS (ºC)	R^2
Clear sky	1078	3.32	2.66	0.06	0.86
Cloudy sky	1213	4.83	3.99	2.11	0.74

4.4. Comparison with two all-weather LST data products

PTM LST and RTM LST were the two all-weather MODIS LST datasets created by merging

MODIS/Aqua LST data with the microwave and reanalysis data, respectively, based on different fusion methods. The interpolated results of this study (the 2nd column of Fig. 12) outperformed the PTM LST data (rightmost column of Fig. 12) in terms of the spatial patterns and image textures, as evidenced by the very blurred textures of PTM LST, in particular, in the central QTP areas on the four arbitrarily selected days. The poor performance of PTM LST regarding the spatial patterns may be related to the use of AMSR2 data in its algorithm, which has a low spatial resolution (0.1°) and limited accuracy (Duan et al., 2020). There were also apparent differences between our results and RTM LST. The interpolated values of this study were lower than those of RTM LST in many regions, such as northwestern QTP in the images on days 70 (the 1st row of Fig. 12) and 5 (the 4th row of Fig. 12) of 2009, represented by a bluer color in the images resulting from this study.

As shown in Fig. 12, the LST values in some regions were particularly different across the three LST datasets. We examined two typical subregions (R1 and R2) in detail. Fig. 13 shows the magnified LST images of the two subregions, with the first and second columns showing the LST distributions of the three sources in subregion R1 on day 70 and R2 on day 5 of 2009, respectively. The rightmost column in Fig. 13 shows the LST histograms for subregion R2, excluding glaciers and lakes. Based on the enhanced details in the two subregions, it was clear that the spatial patterns of LST in both subregions were poorly characterized by PTM LST (the 3rd row of Fig. 13), as indicated by the anomalous artifacts appearing in the northeastern part of subregion R1 and the overall blurry textures in both subregions in the PTM LST images. The interpolated LST values of this study were lower, characterized by cooler tones (the 1st row of Fig. 13), than the LST values of RTM LST and PTM LST in both subregions.

Subregion R2 was a small region surrounding glaciers in northwestern QTP, with an elevation

range of 4659–6275 m a.s.l. In this region, negative LSTs prevailed in winter. Our results represented the characteristics of negative LSTs in this region on a winter day (the 5th day of 2009). The median LST value of our result in subregion R2 was -6.63 ºC for the 5th day of 2009 (Fig. 13g), whereas the those of RTM LST (Fig. 13h) and PTM LST (Fig. 13i) in the same region were 0.76 ºC and 0.73 ºC, respectively, which were unrealistic.

Table 4 lists the accuracy metrics of these data compared to the *in-situ* cloudy-sky LST measurements at the representative QTP sites. Our results outperformed PTM LST in terms of all the performance metrics. PTM LST showed an overestimation for all the six representative sites (BIAS = 3.45 ºC), whereas the BIAS value of our results was 2.11 ºC. The percent BIAS (PBIAS) of PTM LST (25.30%) was higher than that of our results (15.70%). Our results led to the RMSE (4.83 ºC) and MAE (3.90 ºC) values comparable to those of RTM LST (RMSE = 4.85 ºC; MAE = 3.99 ºC). Our results outperformed RTM LST in terms of the BIAS and PBIAS values, 2.11 ºC and 15.70% in this study compared to 2.38 ºC and 17.90% in RTM LST, respectively. Our results resulted in a higher R^2 value (0.74) than that of RTM LST (0.69). In other words, our results were in closer agreement with the *in-situ* cloudy-sky LST observations than RTM LST results. Overall, these cross-comparisons demonstrated that the interpolated results of this study outperformed the two existing all-weather LST products in terms of all the performance metrics of spatial distribution (Fig. 12), seasonal characteristics (Fig. 13), and quantitative evaluation (Table 4).

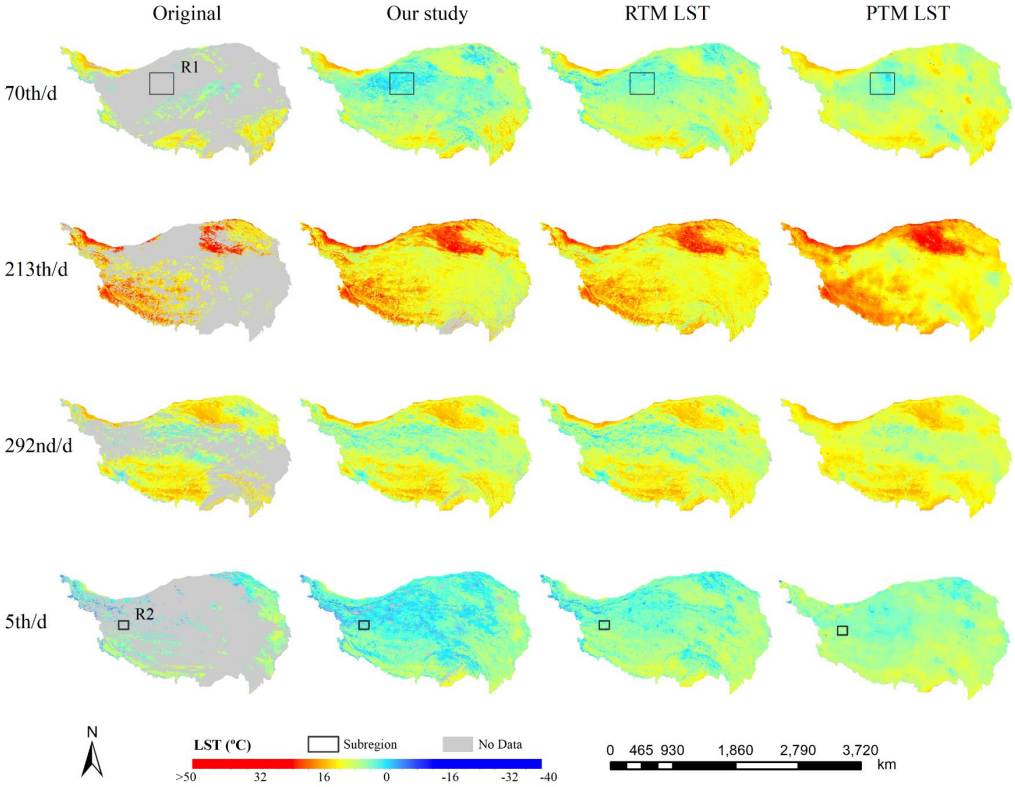

Fig. 12 Comparison of interpolated results of this study with the two all-weather LST products over QTP, i.e., RTM LST fused with reanalysis data (Zhang et al., 2021) and PTM LST fused with microwave data (Xu and Cheng 2021), alongside the original MODIS/Aqua daytime LST images containing extensive null pixels. Both products are based on the MODIS/Aqua LST data. Four days (the 70th, 213th, 292nd, and 5th) in 2009 were arbitrarily selected to represent the different seasons of 2009. Two subregions marked as R1 and R2 were further investigated.

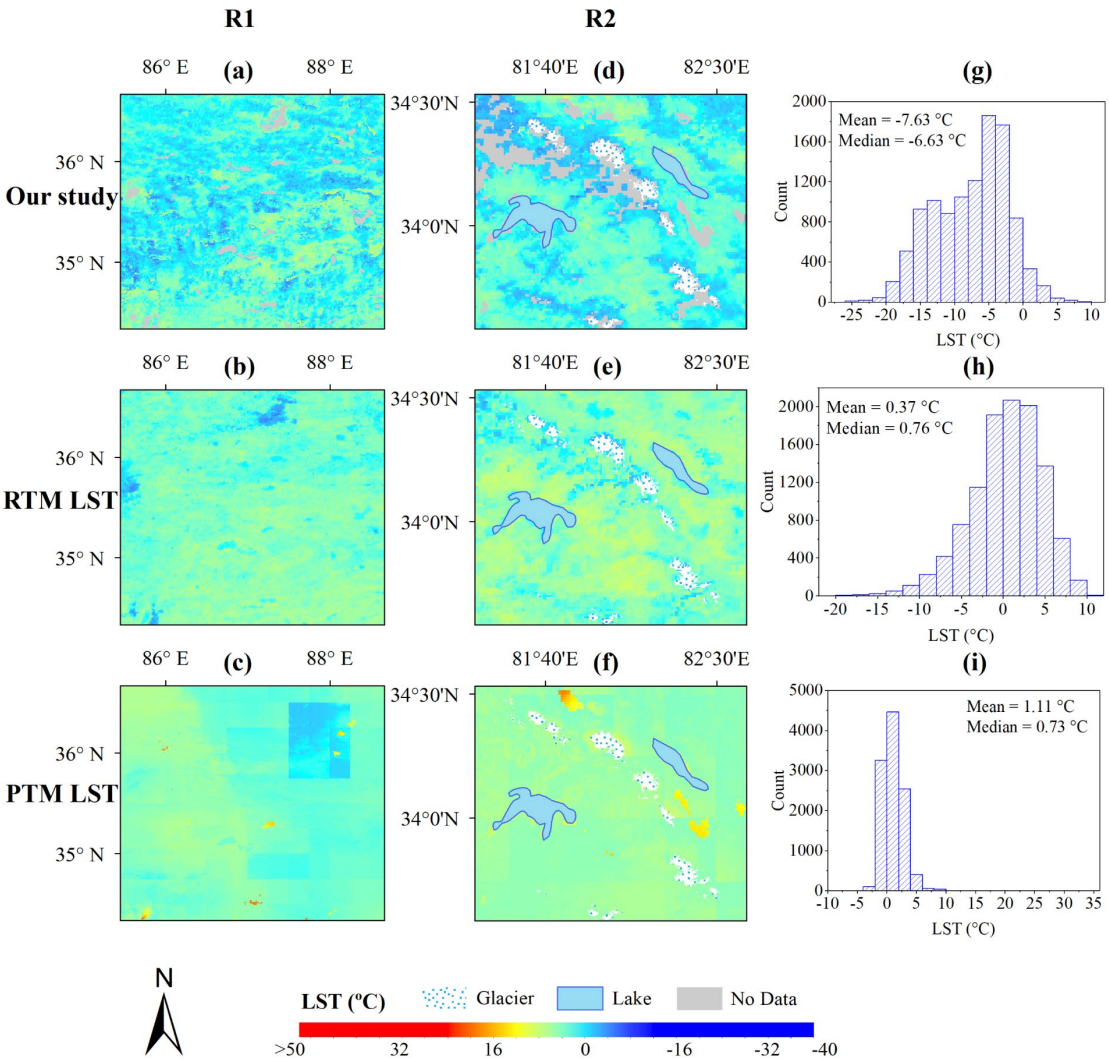

Fig. 13 Spatial details of the LST distributions of two typical regions based on the interpolated results of this study, RTM LST, and PTM LST. R1 and R2 are small regions on the 70th (a-c) and 5th (d-f) MODIS/Aqua daytime LST images of 2009, respectively, as delineated in Fig. 12. The rightmost column (g-i) shows histograms of LST in subregion R2, excluding glaciers and lakes.

Table 4 Accuracy metrics of the interpolated results of this study, PTM LST and RTM LST, versus the *in-situ* cloudy-sky LST measurements at the six representative sites of QTP (n = 1213). The numbers in bold face represent the closest agreement. PBIAS: percent BIAS.

Dataset	RMSE (ºC)	MAE (ºC)	BIAS (ºC)	PBIAS (%)	R^2

PTM	5.14	4.23	3.45	25.3	0.63
RTM	4.85	3.99	2.38	17.9	0.69
Our study	**4.83**	**3.99**	**2.11**	**15.7**	**0.74**

5. Discussion

Unlike most existing approaches, the stepwise approach proposed in this study initially estimated the clear-sky LST equivalents for all the cloud-affected pixels and then recovered the missing cloudy-sky LST values by accounting for cloud effects based on the SCSG effect. This framework is flexible enough to accommodate any clear-sky interpolation methods in the first step (Metz et al., 2014; Neteler 2010; Yu et al., 2015) and any machine-learning algorithms that account for cloud effects on LST as well as the SCSG-based method in the final step. We demonstrated our approach over QTP with vast drylands and complex terrains and compared the results with the two all-weather LST datasets generated from the different data fusion approaches. The results show that the proposed interpolation approach satisfactorily performed for missing cloudy-sky LST pixels over a vast and complex terrain although its accuracy was slightly worse than that of the clear-sky MODIS LST. This was acceptable because the latter provided the highest possible accuracy that could be achieved by our approach. The proposed approach outperformed the two all-weather LST datasets in terms of all the performance metrics of image texture, LST seasonality, and quantitative evaluation. Most strikingly, the proposed approach exhibited a robust ability to handle extensive missing data, primarily attributed to the use of a similarity-based approach to estimate the clear-sky LST equivalents in the first step, which made adequate use of spatiotemporal information (Chen et al., 2021). Thus, the interpolated cloudy-sky LST values leveraged the quality of the clear-sky LST equivalents to reproduce the LST spatial patterns over the large data-gap regions. Except for the *in-*

situ data used to correct biases in the LST values on the cloudy-sky pixels in region D, the inputs to the proposed approach were all from the MODIS family data, without the need for exogenous data. This feature was beneficial for maximizing the data availability in light of the global coverage provided by MODIS as well as for reducing uncertainties arising from spatiotemporal scale mismatches, thus rendering the approach most suitable for regions suffering from heavy cloud contamination and sparse *in-situ* monitoring sites.

This study makes innovative use of cloudy-sky pixels with known LST values owing to the SCSG effect in the same MODIS LST image where the interpolated pixels are located. It is commonly believed that the presence of LST pixels under cloudy skies in a MODIS LST image reduces its overall accuracy (Bulgin et al., 2018; Göttsche et al., 2013). Not surprisingly, the official MODIS LST team planned to completely remove these pixels from LST data products (Wan, 2008). However, our experiments showed that, although the known cloudy-sky LST pixels identified by the SCSG effect had negative biases compared to their actual counterparts at the representative sites, these negative biases could be effectively eliminated and proved to be useful for providing samples that accounted for cloud effects on LST at the same spatiotemporal scale as the satellite data. We found a significantly strong correlation between the satellite and *in-situ* cloudy-sky LST data (R = 0.92). Although a simple linear model appears to be sufficient to achieve acceptable accuracy for the satellite-based cloudy-sky LST observations, there still remains room for improvement. For example, we performed bias correction based on the six representative sites of QTP, representing only two land cover types (bare land and alpine desert) mainly located in northern QTP. Since the scarcity of the available LST sites in the study area limited the bias correction, the performance of the bias correction for other land-cover/use types remains to be quantified. The existing negative

bias in these cloudy-sky data may be related to the current emissivity values in the LST retrieval algorithm, which are not applicable to cloudy-sky conditions. As such, further studies are needed to address these issues by improving the algorithms with proper cloudy-sky emissivity parameters as well as conducting more *in-situ* observations for different land uses/covers on a global scale. We urge the MODIS Land Science Team and relevant land surface communities to pay more attention to the potential of these known cloudy-sky LST pixels rather than simply dismissing them.

These known cloudy-sky LST data, after the bias correction, can be used to compensate for the scarcity of *in-situ* cloudy-sky LST observations, in particular, in remote areas without *in-situ* observations, and gain insight into the effects of clouds on LST variations. While many current efforts to validate all-weather LST data heavily rely on *in-situ* cloudy-sky LST observations, such an approach is often subject to inconsistencies in the spatiotemporal scale and path of at-sensor atmospheric transmittance between satellite and *in-situ* LST observations, with the former being directional and with the latter being hemispherical. As an alternative to *in-situ* data, these satellite cloudy-sky LST data could play a role in validation without these weaknesses.

The proposed approach is not limited to the interpolation of the satellite LST. The presence of the SCSG effect can also cause problems in the land surface radiation budget. For example, shortwave downward radiation retrieval may be significantly biased if the SCSG effect is ignored (Wang et al., 2017). A plausible way to solve the issue may be to remove these affected data and then apply a similar approach to the one presented in this study so as to interpolate for them by using unaffected data that can be located through partitioning based on the SCSG effect.

Despite the satisfactory overall performance, the proposed approach still has some limitations that warrant further investigation. First, uncertainties existed associated with the partitioning of the

MODIS LST images into the SCSG regions. To reduce them, we performed the pre- and post-processing of the cloud-top height data and the SCSG-partitioned images. Although these treatments eliminated most of the anomalies, what remained from them in the resulting SCSG images may have affected the interpolation accuracy. Second, the proposed interpolation framework introduced uncertainties concerning the estimates of both the clear-sky LST equivalents and cloudy-sky LSTs. For the cloudy-sky LST estimation, we identified the similar sets of pixels from SCSG region D based on several environmental predictors under the assumption that these pixels were exposed to similar cloud effects, and the LSTs of those pixels followed the same prediction model. In practice, it is likely that the selected similar pixels may not fully satisfy this assumption, depending on the strength of the selected environmental predictors to define the similarity for the cloudy-sky pixels, the number of pixels in SCSG region D, and the ability of these pixels to represent heterogeneous surface conditions (e.g., land use/cover) throughout the study area. Third, this study assumed that cloud shadows were cast on flat regions, which may not be valid for steep slopes, where cloud shadow shapes are likely to be altered to some degree compared to orthogonal casting (Qiu et al., 2017). Therefore, a further investigation of the SCSG effects in areas with steep slopes is required. Fourth, the data quality of the MODIS family products as the inputs to the proposed approach could be another source of uncertainty in the interpolation results. For example, the MYD11 C6 LST product has a RMSE value of 2.3K and exhibits large biases (3–5K) over dryland regions, as reported in several studies (Li et al., 2021; Malakar and Hulley 2016). This type of uncertainty associated with the original data quality could not be reduced by our interpolation approach. Finally, the proposed approach was only tested with the MODIS/Aqua daytime LST data, whereas a recent study indicated that clouds warm the land surface at night (Tan et al., 2021), which warrants an

investigation of the LST interpolation based on nighttime data.

6. Conclusions

In this study, a stepwise interpolation framework was proposed to recover the missing MODIS LST values due to cloud contamination by taking advantage of cloudy-sky pixels with known LST values owing to the SCSG effect. This framework involved the initial estimation of the clear-sky LST equivalents for all the cloud-affected pixels based on a similarity approach and the subsequent training of MARS models on the known cloudy-sky LST pixels in SCSG region D and its application to the prediction of the unknown cloudy-sky LST values of SCSG region C.

These known LST pixels in SCSG region D, shadowed by clouds but observed by satellites, proved to be useful as they contained information about cloud effects at the same resolution as the satellite. Given our case study of QTP, the known cloudy-sky LSTs from the MODIS/Aqua LST dataset were negatively biased by approximately -4.48 ºC but strongly correlated with the *in-situ* QTP measurements with satisfactory accuracy (BIAS = -0.09 ºC; R^2 = 0.70) after the bias removal. This confirmed the usability of the LST values in SCSG region D as the samples to account for cloud effects on LST.

The interpolation results of the four selected MODIS/Aqua daytime LST images of QTP showed that the resultant textural transitions over large data-gap regions were natural, with no significant anomalous artifacts, and the LST seasonality was well reflected. When compared to the *in-situ* measurements of the representative QTP sites, the interpolated cloudy-sky LST values resulted in good accuracy (R^2 = 0.74; MAE = 3.99 ºC), while, as the reference, the clear-sky LST values of MODIS/Aqua showed a R^2 value of 0.86 and a MAE value of 2.66 ºC. Cross-validation of the results against the two recently published all-weather LST datasets with the different

interpolation approaches indicated that the proposed interpolation approach outperformed both in terms of all the performance metrics of image texture, LST seasonality, and quantitative evaluation.

This study provides a flexible and effective framework for leveraging the existing clear-sky interpolation algorithms to better estimate the missing satellite cloudy-sky LSTs. It also makes innovative use of the readily available cloudy-sky LST values in a satellite LST image owing to the SCSG effect, in particular suitable for areas with sparse *in-situ* LST-monitoring sites or extensive missing LSTs. The SCSG effect can be leveraged to produce high-quality all-weather LST data.

Acknowledgements

This work was supported by National Natural Science Foundation of China under grants 41971074 and 42171125. The first author also received support from the Postgraduate Research & Practice Innovation Program of Jiangsu Province (KYCX22_1563). The in-situ observation data come from Coordinated Enhanced Observing Period, National Tibetan Plateau Data Center (https://data.tpdc.ac.cn/) and National Cryosphere Desert Data Center (http://www.ncdc.ac.cn). The authors would also like to thank the National Aeronautics and Space Administration (NASA) for providing the publicly available MODIS and ASTER data.

Declaration of competing interest

The authors declare that they have no known competing financial interests or personal relationships that could have appeared to influence the work reported in this paper.

Contributions

Conceptualization: Z.N. and Y.C.; Methodology: Y.C. and Z.N.; Software: Y.C. and Z.C.; Validation: Y.C. and K.F.; Supervision: Z.N.; Resources: Z.N.; Writing – original draft: Y.C., Z.N., Z.C. and M.O.; Writing – review & editing: Z.N. and Y.C..

References

Alvera-Azcárate, A., Barth, A., Rixen, M., Beckers, J. M., 2005. Reconstruction of incomplete oceanographic data sets using empirical orthogonal functions: application to the Adriatic Sea surface temperature. Ocean Model. 9, 325-346.

An, Y., Meng, X., Zhao, L., Li, Z., Wang, S., Shang, L., Chen, H., Lyu, S., Li, G., Ma, Y., 2020. Performance of GLASS and MODIS satellite albedo products in diagnosing albedo variations during different time scales and special weather conditions in the Tibetan Plateau. Remote Sens. 12, 2456.

Anderson, M. C., Norman, J. M., Kustas, W. P., Houborg, R., Starks, P. J., Agam, N., 2008. A thermal-based remote sensing technique for routine mapping of land-surface carbon, water and energy fluxes from field to regional scales. Remote Sens. Environ. 112, 4227-4241.

Baraldi, A., Tiede, D., 2018. AutoCloud+, a "universal" physical and statistical model-based 2D spatial topology-preserving software for cloud/cloud-shadow detection in multi-sensor single-date earth observation multi-spectral imagery—Part 1: Systematic ESA EO level 2 product generation at the ground segment as broad context. ISPRS Int. J. Geo-Inf. 7, 457.

Beckers, J. M., Rixen, M., 2003. EOF calculations and data filling from incomplete oceanographic data sets. J. Atmos. Ocean. Technol. 20, 1836-1856.

Brunsell, N. A., Gillies, R. R., 2003. Length scale analysis of surface energy fluxes derived from remote sensing. J. Hydrometeorol. 4, 1212-1219.

Bulgin, C., Merchant, C., Ghent, D., Klüser, L., Popp, T., Poulsen, C., Sogacheva, L., 2018. Quantifying uncertainty in satellite-retrieved land surface temperature from cloud detection errors. Remote Sens. 10, 616.

Chen, Y., Nan, Z., Zhao, S., Xu, Y., 2021. A Bayesian approach for interpolating clear-sky MODIS land

surface temperatures on areas with extensive missing data. IEEE J. Sel. Top. Appl. Earth Observ. Remote Sens. 14, 515-528.

Cheng, J., Liang, S., Yao, Y., Zhang, X., 2013. Estimating the optimal broadband emissivity spectral range for calculating surface longwave net radiation. IEEE Geosci. Remote Sens. Lett. 10, 401-405.

Coll, C., Caselles, V., Galve, J. M., Valor, E., Niclòs, R., Sánchez, J. M., Rivas, R., 2005. Ground measurements for the validation of land surface temperatures derived from AATSR and MODIS data. Remote Sens. Environ. 97, 288-300.

Collins, G. Q., Heaton, M. J., Hu, L., 2019. Physically constrained spatiotemporal modeling: generating clear-sky constructions of land surface temperature from sparse, remotely sensed satellite data. J. Appl. Stat., 1-21.

Deng, Y., Wang, S., Bai, X., Tian, Y., Wu, L., Xiao, J., Chen, F., Qian, Q., 2018. Relationship among land surface temperature and LUCC, NDVI in typical karst area. Sci. Rep. 8, 641.

Duan, S., Han, X., Huang, C., Li, Z., Wu, H., Qian, Y., Gao, M., Leng, P., 2020. Land surface temperature retrieval from passive microwave satellite observations: State-of-the-art and future directions. Remote Sens. 12, 2573.

Duan, S., Li, Z., Li, H., Göttsche, F., Wu, H., Zhao, W., Leng, P., Zhang, X., Coll, C., 2019. Validation of collection 6 MODIS land surface temperature product using in situ measurements. Remote Sens. Environ. 225, 16-29.

Dumitrescu, A., Brabec, M., Cheval, S., 2020. Statistical gap-filling of SEVIRI land surface temperature. Remote Sens. 12, 1423.

Ermida, S. L., Trigo, I. F., DaCamara, C. C., Jiménez, C., Prigent, C., 2019. Quantifying the clear-sky bias of satellite land surface temperature using microwave-based estimates. Journal of geophysical

research. Atmospheres 124, 844-857.

Göttsche, F., Olesen, F., Bork-Unkelbach, A., 2013. Validation of land surface temperature derived from MSG/SEVIRI with in-situ measurements at Gobabeb, Namibia. Int. J. Remote Sens. 34, 3069-3083.

Hagihara, Y., Okamoto, H., Yoshida, R., 2011. Development of a combined CloudSat-CALIPSO cloud mask to show global cloud distribution. Journal of geophysical research 115.

Huang, X., Xie, H., Liang, T., Yi, D., 2011. Estimating vertical error of SRTM and map-based DEMs using ICESat altimetry data in the eastern Tibetan Plateau. Int. J. Remote Sens. 32, 5177-5196.

Jia, A., Ma, H., Liang, S., Wang, D., 2021. Cloudy-sky land surface temperature from VIIRS and MODIS satellite data using a surface energy balance-based method. Remote Sens. Environ. 263, 112566.

Jin, M., 2000. Interpolation of surface radiative temperature measured from polar orbiting satellites to a diurnal cycle: 2. Cloudy-pixel treatment. Journal of Geophysical Research: Atmospheres 105, 4061-4076.

Kasten, F., Czeplak, G., 1980. Solar and terrestrial radiation dependent on the amount and type of cloud. Sol. Energy 24, 177-189.

Kumar, L., Skidmore, A. K., Knowles, E., 1997. Modelling topographic variation in solar radiation in a GIS environment. Int. J. Geogr. Inf. Sci. 11, 475-497.

Kumar, M., Garg, D. P., Zachery, R. A., 2007. A method for judicious fusion of inconsistent multiple sensor data. IEEE Sens. J. 7, 723-733.

Kustas, W., Anderson, M., 2009. Advances in thermal infrared remote sensing for land surface modeling. Agric. For. Meteorol. 149, 2071-2081.

Li, H., Li, R., Yang, Y., Cao, B., Bian, Z., Hu, T., Du, Y., Sun, L., Liu, Q., 2021. Temperature-based and radiance-based validation of the collection 6 MYD11 and MYD21 land surface temperature products

over barren surfaces in northwestern China. IEEE Trans. Geosci. Remote Sensing 59, 1794-1807.

Li, X., Zhou, Y., Asrar, G. R., Zhu, Z., 2018. Creating a seamless 1 km resolution daily land surface temperature dataset for urban and surrounding areas in the conterminous United States. Remote Sens. Environ. 206, 84-97.

Li, Z., Tang, B., Wu, H., Ren, H., Yan, G., Wan, Z., Trigo, I. F., Sobrino, J. A., 2013. Satellite-derived land surface temperature: Current status and perspectives. Remote Sens. Environ. 131, 14-37.

Liang, S., Zhao, X., Liu, S., Yuan, W., Cheng, X., Xiao, Z., Zhang, X., Liu, Q., Cheng, J., Tang, H., Qu, Y., Bo, Y., Qu, Y., Ren, H., Yu, K., Townshend, J., 2013. A long-term Global LAnd Surface Satellite (GLASS) data-set for environmental studies. Int. J. Digit. Earth 6, 5-33.

Long, D., Yan, L., Bai, L., Zhang, C., Li, X., Lei, H., Yang, H., Tian, F., Zeng, C., Meng, X., Shi, C., 2020. Generation of MODIS-like land surface temperatures under all-weather conditions based on a data fusion approach. Remote Sens. Environ. 246, 111863.

Lu, L., Venus, V., Skidmore, A., Wang, T., Luo, G., 2011. Estimating land-surface temperature under clouds using MSG/SEVIRI observations. Int. J. Appl. Earth Obs. Geoinf. 13, 265-276.

Ma, Y., Hu, Z., Xie, Z., Ma, W., Wang, B., Chen, X., Li, M., Zhong, L., Sun, F., Gu, L., Han, C., Zhang, L., Liu, X., Ding, Z., Sun, G., Wang, S., Wang, Y., Wang, Z., 2020. A long-term (2005-2016) dataset of hourly integrated land-atmosphere interaction observations on the Tibetan Plateau. Earth Syst. Sci. Data 12, 2937-2957.

Ma, Y., Yao, T., Wang, J., 2006. Experimental study of energy and water cycle in Tibetan plateau: the progress introduction on the study of GAME/Tibet and CAMP/Tibet. Plateau Meteorol 25, 178-185.

Malakar, N. K., Hulley, G. C., 2016. A water vapor scaling model for improved land surface temperature and emissivity separation of MODIS thermal infrared data. Remote Sens. Environ. 182, 252-264.

Mao, K., Yuan, Z., Zuo, Z., Xu, T., Shen, X., Gao, C., 2019. Changes in global cloud cover based on remote sensing data from 2003 to 2012. Chin. Geogr. Sci. 29, 306-315.

Martins, J. P. A., Trigo, I. F., Ghilain, N., Jimenez, C., Göttsche, F., Ermida, S. L., Olesen, F., Gellens-Meulenberghs, F., Arboleda, A., 2019. An all-weather land surface temperature product based on MSG/SEVIRI observations. Remote Sens. 11, 3044.

Masuoka, E., Fleig, A., Wolfe, R. E., Patt, F., 1998. Key characteristics of MODIS data products. IEEE Trans. Geosci. Remote Sensing 36, 1313-1323.

Metz, M., Rocchini, D., Neteler, M., 2014. Surface temperatures at the continental scale: Tracking changes with remote sensing at unprecedented detail. Remote Sens. 6, 3822-3840.

Mo, Y., Xu, Y., Chen, H., Zhu, S., 2021. A review of reconstructing remotely sensed land surface temperature under cloudy conditions. Remote Sens. 13, 2838.

Muñoz-Sabater, J., Dutra, E., Agustí-Panareda, A., Albergel, C., Arduini, G., Balsamo, G., Boussetta, S., Choulga, M., Harrigan, S., Hersbach, H., Martens, B., Miralles, D. G., Piles, M., Rodríguez-Fernández, N. J., Zsoter, E., Buontempo, C., Thépaut, J., 2021. ERA5-Land: a state-of-the-art global reanalysis dataset for land applications. Earth Syst. Sci. Data 13, 4349-4383.

Neteler, M., 2010. Estimating daily land surface temperatures in mountainous environments by reconstructed MODIS LST data. Remote Sens. 2, 333-351.

Østby, T. I., Schuler, T. V., Westermann, S., 2014. Severe cloud contamination of MODIS land surface temperatures over an Arctic ice cap, Svalbard. Remote Sens. Environ. 142, 95-102.

Palaniyandi, M., Manivel, P., Sharmila, T., Thirumalai, P., 2021. The use of Multispectral (MSS) and Synthetic Aperture Radar (SAR) microwave remote sensing data to study environment variables, land use/land cover changes, and recurrent weather condition for forecast malaria: A review”.

Journal of Applied Ecology and Environmental Sciences 9, 490-501.

Prigent, C., Jimenez, C., Aires, F., 2016. Toward "all weather," long record, and real-time land surface temperature retrievals from microwave satellite observations. Journal of Geophysical Research: Atmospheres 121, 5699-5717.

Qiu, S., He, B., Zhu, Z., Liao, Z., Quan, X., 2017. Improving Fmask cloud and cloud shadow detection in mountainous area for Landsats 4-8 images. Remote Sens. Environ. 199, 107-119.

Rodell, M., Houser, P. R., Jambor, U., Gottschalck, J., Mitchell, K., Meng, C. J., Arsenault, K., Cosgrove, B., Radakovich, J., Bosilovich, M., Entin, J. K., Walker, J. P., Lohmann, D., Toll, D., 2004. The global land data assimilation system. Bull. Amer. Meteorol. Soc. 85, 381-394.

Ryu, Y., Kang, S., Moon, S., Kim, J., 2008. Evaluation of land surface radiation balance derived from moderate resolution imaging spectroradiometer (MODIS) over complex terrain and heterogeneous landscape on clear sky days. Agric. For. Meteorol. 148, 1538-1552.

Sajadi, P., Sang, Y., Gholamnia, M., Bonafoni, S., Brocca, L., Pradhan, B., Singh, A., 2021. Performance evaluation of long NDVI timeseries from AVHRR, MODIS and Landsat sensors over landslide-prone locations in Qinghai-Tibetan Plateau. Remote Sens. 13, 3172.

Shi, C., Xie, Z., Qian, H., Liang, M., Yang, X., 2011. China land soil moisture EnKF data assimilation based on satellite remote sensing data. Science China Earth Sciences 54, 1430-1440.

Shwetha, H. R., Kumar, D. N., 2015. Prediction of land surface temperature under cloudy conditions using microwave remote sensing and ANN. Aquatic Procedia 4, 1381-1388.

Tan, J., Che, T., Wang, J., Liang, J., Zhang, Y., Ren, Z., 2021. Reconstruction of the daily MODIS land surface temperature product using the two-step improved similar pixels method. Remote Sens. 13, 1671.

Tang, W., Xue, D., Long, Z., Zhang, X., Zhou, J., 2022. Near-real-time estimation of 1-km all-weather land surface temperature by integrating satellite passive microwave and thermal infrared observations. IEEE Geosci. Remote Sens. Lett. 19, 1-5.

Tian, F., Qiu, G. Y., Yang, Y. H., Xiong, Y. J., Wang, P., 2012. Studies on the relationships between land surface temperature and environmental factors in an inland river catchment based on geographically weighted regression and MODIS data. IEEE J. Sel. Top. Appl. Earth Observ. Remote Sens. 5, 687-698.

Tomlinson, C. J., Chapman, L., Thornes, J. E., Baker, C., 2011. Remote sensing land surface temperature for meteorology and climatology: a review. Meteorol. Appl. 18, 296-306.

Van De Kerchove, R., Lhermitte, S., Veraverbeke, S., Goossens, R., 2013. Spatio-temporal variability in remotely sensed land surface temperature, and its relationship with physiographic variables in the Russian Altay Mountains. Int. J. Appl. Earth Obs. Geoinf. 20, 4-19.

Wan, Z., 2008. New refinements and validation of the MODIS Land-Surface Temperature/Emissivity products. Remote Sens. Environ. 112, 59-74.

Wang, G., Wang, T., Xue, H., 2021. Validation and comparison of surface shortwave and longwave radiation products over the three poles. Int. J. Appl. Earth Obs. Geoinf. 104, 102538.

Wang, T., Shi, J., Husi, L., Zhao, T., Ji, D., Xiong, C., Gao, B., 2017. Effect of solar-cloud-satellite geometry on land surface shortwave radiation derived from remotely sensed data. Remote Sens. 9, 690.

Wang, T., Shi, J., Ma, Y., Husi, L., Comyn Platt, E., Ji, D., Zhao, T., Xiong, C., 2019. Recovering land surface temperature under cloudy skies considering the solar-cloud-satellite geometry: Application to MODIS and Landsat‐8 data. Journal of Geophysical Research: Atmospheres 124, 3401-3416.

Williamson, S. N., Hik, D. S., Gamon, J. A., Kavanaugh, J. L., Koh, S., 2013. Evaluating cloud contamination in clear-Sky MODIS Terra daytime land surface temperatures using ground-based meteorology station observations. J. Clim. 26, 1551-1560.

Xu, S., Cheng, J., 2021. A new land surface temperature fusion strategy based on cumulative distribution function matching and multiresolution Kalman filtering. Remote Sens. Environ. 254, 112256.

Yang, G., Sun, W., Shen, H., Meng, X., Li, J., 2019. An integrated method for reconstructing daily MODIS land surface temperature data. IEEE J. Sel. Top. Appl. Earth Observ. Remote Sens. 12, 1026-1040.

Yang, X., Ge, J., Hu, X., Wang, M., Han, Z., 2021. Cloud-top height comparison from multi-satellite sensors and ground-based cloud radar over SACOL site. Remote Sens. 13, 2715.

Yu, W., Nan, Z., Wang, Z., Chen, H., Wu, T., Zhao, L., 2015. An effective interpolation method for MODIS land surface temperature on the Qinghai-Tibet Plateau. IEEE J. Sel. Top. Appl. Earth Observ. Remote Sens. 8, 4539-4550.

Yu, W., Tan, J., Ma, M., Li, X., She, X., Song, Z., 2019. An effective similar-pixel reconstruction of the high-frequency cloud-covered areas of southwest China. Remote Sens. 11, 336.

Zhang, H., Zhang, F., Zhang, G., He, X., Tian, L., 2016. Evaluation of cloud effects on air temperature estimation using MODIS LST based on ground measurements over the Tibetan Plateau. Atmos. Chem. Phys. 16, 13681-13696.

Zhang, X., Zhou, J., Liang, S., Wang, D., 2021. A practical reanalysis data and thermal infrared remote sensing data merging (RTM) method for reconstruction of a 1-km all-weather land surface temperature. Remote Sens. Environ. 260, 112437.

Zhao, W., Duan, S., 2020. Reconstruction of daytime land surface temperatures under cloud-covered

conditions using integrated MODIS/Terra land products and MSG geostationary satellite data. Remote Sens. Environ. 247, 111931.